
Capacitance spectroscopy on copper indium diselenide based solar cells

Von der Fakultät für Mathematik
und Naturwissenschaften der
Carl von Ossietzky Universität Oldenburg
zur Erlangung des Grades und Titels eines
Doktors der Naturwissenschaften
(Dr. rer. nat.)
angenommene Dissertation

von
Verena Mertens

geboren am 9.3.1978
in Paderborn

Erstgutachter: Prof. Dr. Jürgen Parisi

Zweitgutachterin: Prof. Dr. Katharina Al-Shamery

Tag der mündlichen Prüfung: 21.12.2005

Abstract

The influence of gallium on the electronically active defects in copper indium diselenide based solar cells is examined. The aim is to clarify whether any detrimental deep levels are responsible for the only sublinear increase in open circuit voltage with increasing band gap for devices with molar gallium to gallium plus indium ratio (GGI) larger than 0.3.

A series of samples with different GGI is investigated using deep level transient and admittance spectroscopy (DLTS and AS). For the solar cells with mixed absorber compositions, i.e., those containing both, gallium and indium, in principle the same defect spectra were found. No fundamental influence of the bulk defects could be identified that causes the "break down" in device efficiencies of solar cells with larger GGI . Furthermore, for the defect signal known as N_1 or β in literature, some remarkable properties are revealed in DLTS measurements. Depending on the respective measurements conditions like the level of reverse bias voltage, height or length of the voltage pulse, either a minority carrier or a majority carrier defect signal is detected, or even a combination of both. The experimental findings cannot be explained by the overlap of two independent trap signals. Two other possible mechanisms are discussed. Additionally, a peak width analysis was performed for these defect signals. No clear relationship between the peak broadening and the gallium content could be revealed, but the activation energies determined for the signals investigated show a GGI dependence. The activation energy decreases up to a GGI of 0.28 which corresponds remarkably well to the respective increase in solar cell efficiency up to the same gallium content.

Zusammenfassung

Der Einfluss von Gallium auf die elektronisch aktiven Defekten in Kupferindiumdiselenid basierten Solarzellen wird untersucht. Das Ziel ist festzustellen, ob schädliche tiefe Störstellen im Material für den nur sublinearen Anstieg der Leerlaufspannung mit zunehmender Bandlückenenergie für Bauelemente mit molarem Gallium zu Gallium plus Indium Verhältnis (GGI) größer als 0.3 verantwortlich sind.

Dazu wird eine Probenserie mit unterschiedlichem GGI mittels Transienter Störstellenspektroskopie und Admittanzspektroskopie (deep level transient spectroscopy, DLTS und AS) untersucht. Für die Solarzellen mit gemischten Absorberkompositionen, also solchen, die Gallium und Indium enthalten, werden prinzipiell dieselben Defektspektren gefunden. Es kann kein grundsätzlicher Einfluss der Volumendefekte auf den "Einbruch" des Wirkungsgrades für Solarzellen mit größerem GGI festgestellt werden. Des weiteren treten in den DLTS Untersuchungen einige bemerkenswerte Eigenschaften des in der Literatur als N_1 oder β bekannten Defektsignals zutage. Abhängig von den entsprechenden Messparametern wie dem Wert der Rückwärtsspannung, der Höhe oder der Länge des Spannungspulses, wird entweder ein Minoritäten oder Majoritätensignal detektiert. Manchmal tritt sogar eine Kombination aus beiden Signalen auf. Die experimentellen Befunde lassen sich nicht durch zwei unabhängige Defekte erklären. Es werden zwei mögliche Erklärungsmodelle diskutiert. Zusätzlich wird eine Peakbreitenanalyse für die zuvor genannten Defektsignale vorgestellt. Eine klare Verbindung zwischen Signalverbreiterung und dem Galliumgehalt kann nicht festgestellt werden. Die Aktivierungsenergien der untersuchten Signale zeigen jedoch eine Abhängigkeit vom GGI . Es wird eine Abnahme der Aktivierungsenergien bis zu einem Galliumgehalt von 0.28 beobachtet, was erstaunlich gut mit dem Anstieg der Effizienz von $\text{Cu}(\text{In,Ga})\text{Se}_2$ Solarzellen bis zu eben diesem GGI korrespondiert.

Contents

1	Introduction	1
2	On $\text{CuIn}_{1-x}\text{Ga}_x\text{Se}_2$ based solar cells	3
2.1	General structure	3
2.1.1	Glass substrate	4
2.1.2	Molybdenum back contact	4
2.1.3	$\text{Cu}(\text{In,Ga})\text{Se}_2$ absorber	5
2.1.4	CdS buffer layer	6
2.1.5	window layer (i-ZnO/Al:ZnO)	7
2.2	The indium-gallium alloy system	7
2.2.1	The open circuit voltage problem	7
2.2.2	Gallium content dependent structural and electrical changes	8
3	Deep levels in semiconductor devices	11
3.1	The space charge region	11
3.2	Electrically active centers	13
3.3	Shockley-Read-Hall theory	14
3.4	Transient trap response	15
3.5	Principle of detailed balance and thermal emission	16
4	Experimental Techniques	21
4.1	The a.c. equivalent circuit of Schottky and p-n diodes	21
4.2	Admittance spectroscopy	22
4.3	Deep level transient spectroscopy (DLTS)	25
4.3.1	General principle: majority carrier DLTS	25
4.3.2	Minority carrier DLTS	29
4.3.3	Reverse bias DLTS (RD LTS)	31
4.3.4	Evaluation with a weighting function	32
4.3.5	Non-exponential transients	35
4.3.6	Devices with non-negligible series resistance	38
4.3.7	Minority carrier defect signals in majority carrier DLTS	39
4.4	Compensation law or Meyer-Neldel rule	39

4.5	The experimental setup	40
5	Experimental Results	41
5.1	Experimental conditions	41
5.2	Defect spectra of the $\text{CuIn}_{1-x}\text{Ga}_x\text{Se}_2$ alloy system	41
5.2.1	Devices with mixed absorber composition	42
5.2.2	CuInSe_2 and CuGaSe_2 based devices	45
5.3	The defect signals below 200 K	48
5.3.1	CuInSe_2 and $\text{Cu}(\text{In,Ga})\text{Se}_2$ absorbers with different gal- lium content	48
5.3.2	Check of signal direction	53
5.3.3	CuGaSe_2 absorbers	54
5.3.4	Peak width analysis	56
6	Discussion	59
6.1	The defect spectra of the In-Ga alloy system	59
6.2	The trap signals E_1 and H_1	62
6.3	Peak width analysis of E_1 and H_1	66
7	Conclusions	69
	Bibliography	71

Chapter 1

Introduction

During the last 20 years the interest in thin film solar cells has steadily increased. The reasons for this development are at hand: although silicon based solar cells do still exhibit the highest efficiencies, their cost of production is still quite high even if polycrystalline material is used. Here, two main reasons have to be mentioned. The first is that crystalline silicon is an indirect semiconductor. To absorb the incident light sufficiently, the absorber layer has to be about 100 to 200 μm thick. This is quite a lot compared to other materials with a direct band gap. The second aspect is actually a consequence of the aforementioned one. As the silicon devices have to have a thickness of a few hundred micrometers, the material has to be very pure to obtain high efficiency devices. Otherwise the impurities of the material function as traps and recombination centers so that the extra electrons and holes created by absorption of light could hardly reach the contacts and provide electrical energy. Additionally large area modules that are indispensable for real life applications of solar cells have to be constructed by connecting single devices in an elaborate process. There is hope that these shortcomings can be met by thin film solar cells so that their still comparatively low efficiencies can be compensated. At the moment, thin film solar cells based on copper indium gallium diselenide (CIGS) are the most promising candidates. They exhibit the highest record efficiencies of thin film devices, 19.2 % on laboratory cells [1] and 14.3 % on modules [2]. As the material is a direct semiconductor, the absorber layer has to be only about 1.5 μm thick. They can easily be produced for instance by physical vapour deposition of the constituent elements. The area of the active layer can be adjusted to the appropriate size without serious problems because of the relative easy way of production. To obtain modules, the different layers which form the solar cell are deposited on the whole area of the module and can afterwards easily be structured by laser lithography. As the semiconductor material consists of three different compounds, the band gap can also be adjusted in a certain range by variation of the gallium to gallium plus indium ratio (GGI or

gallium content if expressed in percent). The addition of sulfur to enlarge the bandgap is possible, too. CuInSe_2 has a band gap of 0.98 eV, CuGaSe_2 of 1.66 eV [3]. Momentarily the solar cells with the highest efficiency have a gallium content of about 28 % which corresponds to a band gap of about 1.15 eV. However, the best adjustment to the solar spectrum is accomplished by an absorber layer with a band gap of about 1.4 eV to 1.6 eV. Shortly after the first attempts to fine-tune the band gap of the CIGS absorber layer and therewith the open circuit voltage V_{oc} of the resultant devices to the desired value, it was recognized that the open circuit voltage of the solar cells does not increase in the same way as the band gap of the absorber material. The reasons are still not clear. Within this thesis, defect spectroscopy measurements were performed to get an insight into the bulk defects occurring in the indium-gallium alloy system of CIGS and their dependence on the gallium content. The thesis on hand is organised as follows: In Chapter two an overview concerning the $\text{Cu}(\text{In,Ga})\text{Se}_2$ solar cells is given with special focus on the changes due to addition of gallium to the CuInSe_2 absorber layer. Chapter three introduces some theoretical concepts like the space charge region in semiconductor devices and properties of defect states which are necessary to explain the experimental techniques applied within this thesis. In Chapter four, the actual measurement techniques are described. Chapter five describes the experimental results obtained which are afterwards discussed in Chapter six. Finally, the main ideas of the thesis are summarized in Chapter seven along a short outlook for future investigations.

Chapter 2

On $\text{CuIn}_{1-x}\text{Ga}_x\text{Se}_2$ based solar cells

CuInSe_2 and its alloys (CuInSe_2 : CIS, $\text{CuIn}_{1-x}\text{Ga}_x\text{Se}_2$: CIGS or CuGaSe_2 : CGS) belong to the family of chalcopyrites. These materials are direct semiconductors [4, 5, 6], i.e., the conduction band minimum and the valence band maximum occur at the same wave vector so that band-to-band excitation by photons and recombination of charge carriers by photon emission, respectively, are possible, because no absorption or emission of additional phonons is necessary to ensure conservation of momentum. Therefore the probability to absorb photons of energy at least as high as the band gap energy is high for this material and the film can be made thinner than $1.5 \mu\text{m}$. For this reason, the solar cells made of these materials as absorber layer have a thickness of only $3 \mu\text{m}$ and are called "thin film solar cells". In the following, the schematic of the CIGS solar cell will be discussed in terms of processing and functionality of the different layers. Afterwards some details of the indium-gallium alloy system are discussed.

2.1 General structure

The structure of the device is shown in figure 2.1(a). On top of a glass substrate there is the molybdenum back contact, followed by the p-type CIGS (alternatively CIS, CGS) absorber layer. An n-type buffer layer which is formed by cadmium sulfide (CdS) in the devices investigated, separates the CIGS and the actual window layer. The window layer itself consists of an intrinsic zinc oxide (i-ZnO) and an aluminum doped n-type ZnO layer (Al:ZnO). On laboratory cells, an aluminum grid is deposited on top of the whole cell to facilitate contacting the device.

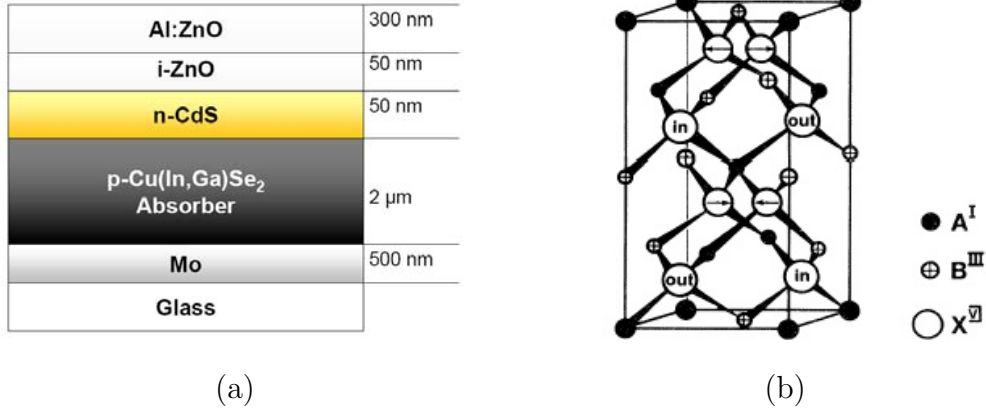


Figure 2.1: (a) Schematic of the $\text{Cu}(\text{In,Ga})\text{Se}_2$ solar cell. (b) The chalcopyrite lattice. The A sites are occupied by the Cu^+ ions and the B places by In^{3+} and/or Ga^{3+} ions. The Se^{2-} or S^{2-} ions occupy the X sites. The anions show a slight displacement compared to the tetrahedral structure which is indicated by the arrows and in-plane and out-of-plane directions [7].

2.1.1 Glass substrate

Usually a sodium containing glass like soda lime glass is taken as substrate. It was recognized that, during absorber deposition, sodium diffuses through the Mo layer into the absorber and has multiple positive influence on the material [8, 9, 10]. During growth, sodium doping leads to a better morphology [11] by retarding of phase formation to higher temperatures [12]. In the material, it is mostly accumulated at grain boundaries [11]. There, the sodium leads presumably to passivation of grain boundaries and increases the p-type conductivity [13]. Another option instead of more or less uncontrolled sodium diffusion into the absorber layer, is the deposition of a Na diffusion barrier on top of the glass substrate and the providence of a defined amount of sodium in form of a precursor like NaF prior to or during deposition of the absorber layer [14, 15].

2.1.2 Molybdenum back contact

The molybdenum is deposited on the glass substrate usually by d.c. magnetron sputtering [16]. Considering the Mo/ $\text{Cu}(\text{In,Ga})\text{Se}_2$ interface, the metal does not diffuse into the absorber material, but forms a thin MoSe_2 film in presence of excess selenium during growth of CIGS [17, 18]. Probably because of this layer, there is only a small potential barrier between molybdenum and CIGS, so that the back contact behaves as ohmic at room temperature.

2.1.3 Cu(In,Ga)Se₂ absorber

The absorber material normally used for CIGS solar cells is an alloy of the two ternary semiconductors CuInSe₂ and CuGaSe₂ with a gallium to indium plus indium ratio GGI of 0.28. The materials in the I-III-VI₂ system are often called chalcopyrites because they have the same crystal structure as the mineral chalcopyrite (CuFeS₂), a common copper-iron ore. The crystal structure is based on the zincblende structure which again is based on the diamond structure. The chalcopyrite lattice is obtained from the zincblende structure by introduction of an additional ordering into the cation sublattice which requires a doubled primitive cell (see figure 2.1). The semiconducting properties of the chalcopyrites are due to their electronic and structural similarity to the group IV semiconductors like silicon or germanium. The zincblende structure is isoelectronic to Si, if the constituent elements are chosen symmetrically from groups to the left and to the right of group IV. Prominent examples are the III-V semiconductors like GaAs, or II-VI semiconductors like ZnSe. Taking the idea one step further by replacing the Zn in ZnSe with the adjacent elements of valency I and III yields the ternary compound CuGaSe₂. The band gap is influenced by two mechanisms: In the isoelectronic series Ge, GaAs, and ZnSe the decreasing covalency (increasing ionicity) of the bonds increases the band gap from 0.7 to 1.4 and 2.7 eV (at 300 K), respectively. Then, going from ZnSe to CuGaSe₂, the band gap is reduced from 2.7 eV to 1.7 eV by the combined effects of spin orbit coupling, the crystal field of the tetragonal structure, and the influence of the Cu-3d electrons on the valence band [19].

CuInSe₂ is amazingly tolerant towards off-stoichiometric composition. This effect is ascribed to formation of defect complexes like $(2 V_{Cu}^- + In_{Cu}^{+2})^0$ (V_{Cu}^- : copper vacancy, In_{Cu}^{+2} : indium on copper site) which are able to passivate large defect concentrations [20]. Addition of sodium and replacement of indium by gallium increase this tolerance further [21]. The properties of the material are generally dominated by native defects resulting from off-stoichiometric material composition. One discriminates copper-poor and copper-rich (molar ratio of copper to indium plus gallium concentration smaller or larger than one) and selenium-poor and -rich conditions (where the ratio of selenium and the metal ion concentrations is smaller or larger than one). The p-type conductivity is mainly attributed to copper vacancies V_{Cu}^- whereas n-type CuInSe₂ is probably due to copper interstitials Cu_i^+ or selenium vacancies V_{Se}^+ . [22, 23]. However, the material is highly compensated, i.e., donor and acceptor-like doping centers do likewise occur [24, 25]. Device grade absorber layers are slightly copper-poor and selenium-rich. The selenium content increases the p-type character, the copper deficiency is necessary to prevent any phase separation as copper-rich material tends to precipitations of Cu_{2-x}Se which is a p-type semiconductor, too [22]. The best

solar cells are made from overall copper-poor CIGS with a Cu content of typically 22 at% to 24 at%. There exist various preparation procedures for the CIGS absorbers [26]. Here, only the two most frequently used processes shall be introduced. The first one is the stacked deposition of the elementary compounds Cu, In, Ga and Se on top of the molybdenum covered glass substrate and subsequent fast annealing under inert gas [27]. This is called "rapid thermal processing". Alternatively, it is also possible to omit the selenium in the deposition step and perform the heating in an H_2Se or Se atmosphere [28]. The second method to process the absorber layer is the co-evaporation from elemental sources on a heated substrate (glass plus Mo back contact), so that the CIGS is formed already during deposition [29]. Up to now, elaborate processes have been developed like the bilayer or the three stage process with alternating copper-poor and copper-rich deposition phases [30, 31] or gallium grading within the absorber layer [32]. The Cu-rich step serves to enlarge the grain size of the material as the grain size increases with increasing copper content [33]. The investigations presented within this thesis are performed on solar cells containing absorbers synthesized by single stage co-evaporation [34].

In the CIGS absorber the actual light to energy conversion process takes place. There is experimental evidence, that the surface of the CIGS layer is copper depleted compared to the composition of the bulk material [35] and therefore has a larger band gap [36]. Additionally it was found that the deposition of the CdS buffer layer leads to heavy Cd doping within the first couple of atomic layers [37]. If the Cd occupied the copper vacancies present within this regime therewith formed donor defects Cd_{Cu}^- , the Cd doping would lead to an increased electron concentration and might induce the suspected type inversion within the surface region [37]. Evidence for such a "buried" homo-junction was given by scanning Kelvin probe force microscopy investigations [38] and other experiments [39, 40].

2.1.4 CdS buffer layer

The n-type CdS buffer is deposited from a chemical bath (CBD process) [41]. As this is the only processing step of the solar cell that is not capable of an inline-production, multiple attempts have been made to replace it by for instance physical vapor deposition. Moreover, the cadmium as toxic element might put the reputation of CIGS solar cells at risk. At last, the band gap of 2.4 eV of the cadmium sulfide impedes the transmission in the short wavelength regime, so that there are several aspects which support its replacement. However, the CBD process is still necessary to produce highly efficient solar cells, so that some groups who work on replacement of CdS aim at cadmium-free buffer layers but retainment of the chemical bath deposition process. There are several materials under investigation, for instance

ZnS [42], $\text{In}(\text{OH})_x\text{S}_y$ [43], MnS [43], ZnSe or SnO_2 . The purpose of this intermediate layer between the absorber and the window layer is still of current interest in research. Some of the beneficial effects of the CBD processed CdS buffer layer identified so far are removal of natural oxides from the CIGS surface [44] and protection of the CIGS layer from negative influences of the sputtering processes used to deposit the window layer. The cadmium diffusion into the CIGS film was already mentioned in section 2.1.3.

2.1.5 window layer (i-ZnO/Al:ZnO)

The window layer consists of an n-type aluminum doped zinc oxide film on top of a thin layer of an intrinsic zinc oxide. Both ZnO films are commonly deposited by sputtering processes. The n-doped zinc oxide provides a highly conductive front contact with a band gap large enough to be transparent in the relevant photon energy range [45]. For intrinsic ZnO E_G is 3.4 eV [45]. For the aluminum doped zinc-oxide the band gap is a little larger [46]. The role of the resistive i-ZnO is still a matter of discussion. It was proposed that it reduces the impact of lateral inhomogeneities due to varying electrical properties of different crystallites [47, 48]. Maybe it also prevents the aluminum from diffusion into the absorber layer.

2.2 The indium-gallium alloy system

After the description of the Cu chalcopyrite solar cell in general, the properties of the material and devices with nonstandard absorber composition are presented. Firstly, the technological relevance and the interest in the enlargement of the band gap energy of the Cu chalcopyrites by gallium or sulfur addition is pointed out. In the second part of this section, a summary of the so far known influence of the gallium content on the material and device properties is given.

2.2.1 The open circuit voltage problem

For a most efficient adjustment to the solar spectrum, absorber materials should have a band gap energy of about 1.4 eV to 1.6 eV. In case of the Cu chalcopyrite solar cells, this could be achieved either by complete replacement of selenium by sulfur to obtain CuInS_2 [49] or by an increase in GGI to about 0.5 to 0.75. However, for both strategies, the solar cell performance reached are so far not satisfactory [50]. Devices with GGI larger than 0.3 exhibit a decrease in efficiency compared to the one achieved for solar cells with standard absorber compositions [51]. It was found that the open circuit voltage increases only sublinear with increasing band gap energy [52, 53].

For the sulfur containing solar cells the "V_{OC} breakdown" is not abrupt but happens slowly with increasing sulfur concentration. To find out, whether this problem is a general material property or is caused by the interplay of the different layers that form the structure of the CIGS solar cell, many investigations have been made to get more insight into the gallium dependent material and device properties and those of CuInS_2 solar cells, respectively. Here, the investigations presented and discussed shall be restricted to the gallium issue as this approach is the one that is more commonly followed. Moreover, the results presented within this thesis focus on the indium-gallium system, too.

2.2.2 Gallium content dependent structural and electrical changes

Concerning the addition of gallium to CuInSe_2 , there are theoretical and experimental studies available. The most obvious modification is of course the increase in band gap energy from 0.98 eV to 1.66 eV. The enlargement of E_G and therewith occurring respective shifts in conduction band minimum and valence band maximum have direct influence on the band offsets between CdS and the absorber layer. For the $\text{CuInSe}_2/\text{CdS}$ heterointerface, valence band offsets of about 0.79 eV to 0.86 eV [54, 40, 55] were determined experimentally which give a positive conduction band offset $\Delta E_c = E_c(\text{CdS}) - E_c(\text{CIS})$, a so called "spike" of about 0.3 eV, assuming a copper-poor CuInSe_2 surface with a band gap of about 1.3 eV and a band gap of 2.4 eV for CdS [40]. On addition of gallium the positive conduction band offset decreases with increasing gallium content and finally develops into a negative one, referred to as "cliff" [56]. This is mainly due to a shift in conduction band minimum. The valence band minimum shows only a slight shift to lower energies [56, 57]. The energy band diagrams for complete solar cells with CuInSe_2 and CuGaSe_2 absorber, respectively, are shown in figure 2.2a and b.

In contrast to CuInSe_2 , where the material is n-type when it is heavily copper-poor and likewise selenium-rich [22], there exists no such phase for CuGaSe_2 . Therefore, a homojunction as exists in the case of CIS can be excluded for CGS [59]. One rather deals with a comparatively rough heterojunction. Together with the changes in band alignments, this might lead to increased interface recombination. However, for copper-poor CuGaSe_2 based solar cells tunneling enhanced bulk recombination was identified as mechanism instead [60]. Concerning the doping concentration for copper-poor CIS and CGS, theory and experiment both find an increase in doping concentration for the copper-poor materials from about 10^{15} cm^{-3} for CuInSe_2 [61] to about 10^{16} cm^{-3} for CuGaSe_2 [60].

There are also studies concerning the changes in bulk defects. Compar-

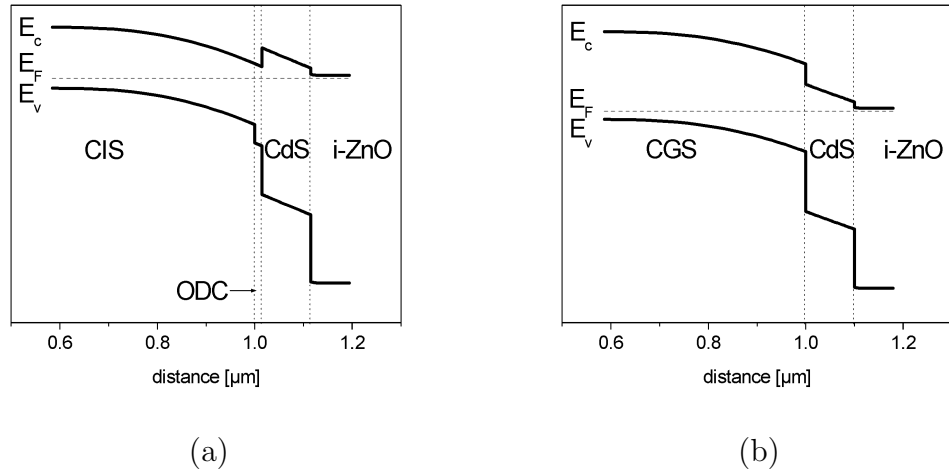


Figure 2.2: (a) Energy band diagram for a CuInSe_2 based solar cell including the copper-poor surface layer indicated as ordered defect compound (ODC). Note the small positive band offset (spike) between CdS and CIS. (The CdS-CIS band offsets are taken from reference [55], other parameters are from the CIGS solar cell definition file provided by SCAPS 1-D [58]). (b) Energy band diagram for a CuGaSe_2 based solar cell. Note the negative band offset (cliff) between CdS and CGS. (The CdS-CGS band offsets are calculated from data of references [55] and [56], other parameters are again from the CIGS definition file provided by SCAPS 1-D [58].)

ative calculations between CuInSe_2 and CuGaSe_2 of their defect formation energies and transition energies for the occurring deep levels indicate, that Ga addition lowers the relative stability of the defect pair $(M_{Cu}^{+2} + 2V_{Cu}^{-})^0$ [57]. The defect complex is assumed to inactivate the deep donor M_{Cu} [20]. Moreover, this defect pair forms the ordered defect compound CuIn_3Se_5 , if it is spatially repeated [20]. The point defects of CuGaSe_2 have about the same defect transition energies as in CuInSe_2 or slightly lower ones, except for the M_{Cu} defects. In this case, the In_{Cu} donor levels with $E_c - 0.25$ eV and $E_c - 0.34$ eV, respectively, are substantially shallower than the Ga_{Cu} levels with $E_c - 0.49$ eV and $E_c - 0.69$ eV, respectively [57].

Some systematic experimental studies on CIGS solar cells with different gallium content are known, too. Photocapacitance measurements disclosed one deep defect occurring for all *GGI* with activation energy of about 0.8 eV [62]. In admittance spectroscopy measurements, two defects were found, again irrespective of the gallium content [63, 64, 65]. For the shallower trap (called N_1) a broad range of activation energies E_a of around 0.05 eV to 0.3 eV was found [63, 64, 65]. For the deeper second trap level which is named N_2 an activation energy of about 0.3 eV was determined [65, 66]. The concentration

of the defect N_2 was found to correlate to the device efficiency [66]. The trap signal N_1 was detected by drive level capacitance measurements, too [67]. Deep level transient spectroscopy investigations of CIGS solar cells with standard absorber composition also disclosed both defect signals, N_1 and N_2 . N_1 was detected as minority carrier signal, whereas N_2 was found to be a majority carrier defect. However, there have been discussions in literature about the origin of defect signal N_1 , because the positive minority signal is visible in majority carrier DLTS, i.e., under non-injection conditions, where usually minority signals are not detected. Crandall et al. [68] identified a majority trap signal for all *GGI* with DLTS .

Within this thesis, a systematic study of the defects in samples with different *GGI* using deep level transient spectroscopy and admittance spectroscopy, is presented. The intention was to complete the picture of changes in defect spectra with varying gallium content to clarify, whether the sub-linear increase in V_{OC} with the band gap is influenced by deep levels in the bulk, e.g., by substantial changes in defect spectra with increasing *GGI*.

Chapter 3

Deep levels in semiconductor devices

In the following sections, a description of the theory necessary to explain the experimental techniques applied within this thesis is given. Firstly, the concept of space charge region is introduced. Afterwards defect states in semiconductors and their properties like recombination kinetics and thermally activated emission are described.

3.1 The space charge region

The depletion region is actually the core of all semiconductor devices. It is the reason for the rectifying behavior which is characteristic of Schottky diodes [69] and p-n junctions. In other devices like elaborate solar cell concepts or transistors [70], one even deals with two or more depletion regions. Generally, the development of a space charge region can be described in terms of equalization of the electrochemical potentials for electrons (or holes) within the two materials that are brought in intimate contact [71]. The process shall be visualized now for electrons in a p-n junction. (For a metal-semiconductor diode, the situation is in principle the same.) The electrochemical potential η_e , which is often referred to as Fermi level in semiconductor physics, is the sum of the chemical potential μ_e and the electrical potential φ . Here the equation for electrons in an n-type semiconductor is given:

$$\eta_e^n = \underbrace{\mu_{e,0}^n}_{\mu_e^n} + kT \ln \frac{n_e^n}{N_C} - q\varphi^n. \quad (3.1)$$

For the two separate semiconductors, the electrical potentials φ^n and φ^p are zero. In this case, the chemical potentials in both layers are equal to the electrochemical potential, e.g., the Fermi energy. As soon as the contact is

formed, electrons start to diffuse from the side of high chemical potential to the one of lower chemical potential. As in most cases the chemical potential of the electrons is larger in the n-type than in the p-type semiconductor, they usually move from the n-doped side into the p-type layer. Respectively, the holes move from the p-type layer to the n-side. These diffusion currents are accompanied by positive charging of the n-side and negative charging on the p-side, respectively. The current flow stops as soon as a electrical potential difference has built up that balances the gradient in chemical potential, so that:

$$\eta_e^n = \eta_e^p \quad (3.2)$$

which is in detail:

$$\mu_e^n - q\varphi^n = \mu_e^p - q\varphi^p. \quad (3.3)$$

One remark has to be made concerning $\mu_{e/h}$. It consists of a constant contribution and a contribution which depends on the actual carrier concentration in the material. The constant part is the standard chemical potential $\mu_{e/h,0}$. It is determined by the chemical environment of the free charge carriers. Generally, the equilibrium potential difference or alternatively called diffusion potential is given by:

$$\varphi^n - \varphi^p = \frac{\mu_{e,0}^n - \mu_{e,0}^p}{q} + \frac{kT}{q} \ln \frac{n_e^n}{n_e^p}. \quad (3.4)$$

For a homojunction, for instance formed by n- and p-type silicon, respectively, the standard chemical potential $\mu_{e/h}^0$ is therefore about the same in the n- and p-doped semiconductor so that the diffusion potential is only determined by the difference in carrier concentrations. In the case of a heterojunction like CdS(n-type)/CIGS(p-type), the standard chemical potentials have to be taken into account. However as for two different semiconductors 1 and 2 the difference in electron affinities $\Delta\chi$ corresponds to the difference in standard chemical potentials $\Delta\mu_{e,0}$:

$$\mu_{e,0}^1 - \mu_{e,0}^2 = \chi^2 - \chi^1, \quad (3.5)$$

and the difference in electrical potentials can still be calculated. For a Schottky diode, the metal work function replaces the electron affinity of the second semiconductor.

The spacial extension of potential difference $\varphi^n - \varphi^p$ into the n- and the p-side of the device, e.g., the width of the space charge region, can be calculated from Poisson's equation

$$-\nabla^2\varphi = \frac{\rho}{\epsilon\epsilon_0}, \quad (3.6)$$

where ρ is the space charge density, ϵ_0 is the permittivity of free space and ϵ is the relative permittivity of the respective semiconductor material. Using a one-dimensional treatment of this problem (infinite extension of the junction in y - and z -direction) and assuming a constant doping concentration (otherwise this problem can be solved only numerically) the width is given by:

$$x_d = \sqrt{\frac{2\epsilon\epsilon_0 N_a + N_a}{q N_a N_d} (\underbrace{\varphi^n - \varphi^p}_{V_d} - V)}. \quad (3.7)$$

N_d and N_a are the donor and acceptor doping concentrations on the n- and on the p-side, respectively, $\varphi^n - \varphi^p$, the difference in electrical potentials is also referred to as "diffusion or built-in potential" V_d , and V is the potential applied additionally to device. If there is a large difference in doping concentration, e.g. free carrier concentration, between the n- and the p-side, the width of depletion region is approximately equal to its extension into the lower doped side of the junction. This is the case for metal-semiconductor diodes, too. One comment has to be made concerning equation 3.7. This expression for the depletion region width is based on the so called "full-depletion" approximation [45]. It means that no free charge carriers are assumed to exist in the depletion region and that the transition from the depleted region to the neutral bulk is abrupt, so that it can be described by a step function. Actually, the free carrier concentration decreases about exponentially at the depletion region edges, but in most cases, the depletion approximation is an appropriate method to simplify calculations.

3.2 Electrically active centers

In semiconductors, not only doping centers do occur but also other electrically active centers that are located closer to mid gap compared to the doping levels. These are called traps or deep levels. Similar to doping levels, one also differentiates between donor-like deep levels which are positively charged when unoccupied by electrons and acceptor-like trap states which are negatively charged when occupied by electrons. The distinction between doping levels and traps depends on many different factors. Usually, shallow centers are ionized already at low temperatures and therefore enlarge the free carrier concentration of the semiconductor. So they are considered to have a positive influence on the material. Deep levels can have a huge influence on the device for example on the charge transport or on the energy band structure. Mostly, their impact on the material or the device is negative. As a rule of thumb, the energetic position of a level within the band gap of the material can be taken as indication of its "character": the closer the defect level is to the

middle of the gap, the more it tends to act as a trap or — even worse — as a recombination center. A more precise definition says, that deep levels exhibit a short-range Coulomb potential whereas shallow dopants have a long-range one. Depending on their occupation and charge state relative to the one of the doping levels, deep traps can enhance or compensate the space charge caused by ionized doping levels within the depletion region. For instance if we deal with a p-type semiconductor, e.g., the doping levels are shallow acceptors, a donor-like deep level compensates the doping concentration when it is unoccupied by electrons (and therefore positively charged) whereas it has no influence on the space charge when it is occupied by electrons (and therefore neutral). With their impact on the space charge, deep traps do also affect the width of the depletion region. The doping concentrations in equation (3.7) are in this case effective concentrations, i.e., the sum of all charged states, shallow and deep. The kinetics of capture and emission processes on a trap level are given by the Shockley-Read-Hall theory.

3.3 Shockley-Read-Hall theory

The Shockley-Read-Hall theory describes recombination of charge carriers via defect states [72, 73]. For a single or point like level within the band gap, four different processes can occur as shown in figure 3.1.

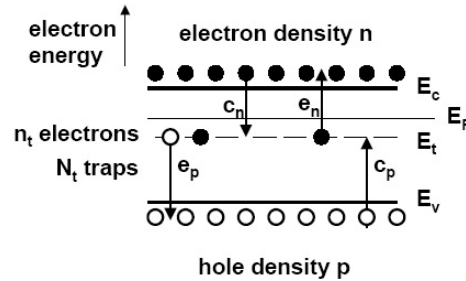


Figure 3.1: Shockley-Read-Hall recombination processes demonstrated for a deep level E_t with density N_t occupied by n_t electrons. Also indicated are the conduction band minimum E_c , the valence band maximum E_v , the Fermi level E_F as well as the electron and hole densities n and p in the respective energy bands.

Generation rates (G):	Recombination rates (R):
emission of electrons: $e_n n_t$	capture of electrons: $c_n p_t$
emission of holes: $e_p p_t$	capture of holes: $c_p n_t$

with:

$$p_t = N_t - n_t, \quad (3.8)$$

$$c_n = \sigma_n v^{th} n. \quad (3.9)$$

$$c_p = \sigma_p v^{th} p. \quad (3.10)$$

Here, the c_n , c_p , e_n and e_p are the capture rates per unoccupied state and emission rates per trapped charge carrier for electrons and holes, respectively ("normalized capture and emission rates"), n_t (p_t) is the number of traps occupied by electrons (holes), N_t is the total number of trap states and n (p) is the free carrier concentrations of electrons (holes) in the conduction band (valence band). The capture rates can be calculated from equations 3.9 and 3.10 as the product of capture cross section $\sigma_{n/p}$, the average thermal velocity of free charge carriers v^{th} which is about 10^{-7} cm/s at 300 K and the free carrier density. The capture cross section is a measure for how effective charger carriers are captured into the specific trap. It is sometimes taken as indication for the charge state of the respective trap relative to the one of the captured charge carrier. Centers with capture cross section larger than 10^{-14} cm² are classified as Coulomb attractive, those with σ in the range from 10^{-16} cm² to 10^{-14} cm² to be neutral and trap states with capture cross sections smaller than about 10^{-17} cm² are categorized as repulsive. With these rates, the change in electron densities given by:

$$\frac{dn}{dt} = G_n - R_n = e_n n_t - c_n p_t. \quad (3.11)$$

Respective expression holds for the hole density, too:

$$\frac{dp}{dt} = G_p - R_p = e_p p_t - c_p n_t. \quad (3.12)$$

3.4 Transient trap response

Using the equations for the change in electron and hole densities, it is possible to calculate the time dependence of the number of occupied traps [74]. Here, the expression is shown for the number of deep levels occupied by electrons. The respective equation for the traps occupied by holes can be obtained by replacement of n_t by $N_t - p_t$.

$$\frac{dn_t}{dt} = G - R = G_p - R_p - (G_n - R_n) = (c_n + e_p)(N_t - n_t) - (c_p + e_n)n_t \quad (3.13)$$

The general solution of this differential equation (assuming the rates c_n, c_p, e_n, e_p to be time independent) with $n_t = n_t(0)$ for $t = 0$ is

$$n_t(t) = n_t(\infty) - \{n_t(\infty) - n_t(0)\} \exp(-t/\tau) \quad (3.14)$$

with the steady state occupancy given by

$$n_t(\infty) = \frac{c_n + e_p}{c_n + e_p + c_p + e_n} N_t \quad (3.15)$$

and τ^{-1} , the rate constant (or inverse time constant τ^{-1}),

$$\tau^{-1} = c_n + e_p + c_p + e_n. \quad (3.16)$$

Equation (3.14) describes the relaxation of the number of traps occupied (in this case by electrons) back to the equilibrium occupancy after perturbation. The process is an exponential decay, where the inverse time constant is the sum of all normalized capture and emission rates. The position of the Fermi level governs the free carrier concentration and therefore has influence on whether a state is occupied or not. Under equilibrium conditions, i.e., when no potential difference is applied to the device, it completely determines the trap occupation. This will be clarified in the next section.

3.5 Principle of detailed balance and thermal emission

The principle of detailed balance says that in thermal equilibrium, the capture and emission rate of electrons and holes, respectively, have to be equal.

$$e_n n_t = c_n (N_t - n_t)$$

and

$$e_p p_t = c_p (N_t - p_t) \quad (3.17)$$

These equations determine also the equilibrium trap occupation. The following derivation of the temperature dependence of the emission rates, will be performed for an electron tap. The respective expressions for holes can again be obtained by replacing n_t with $N_t - p_t$.

$$\frac{n_t}{N_t} = \frac{c_n}{c_n + e_p} = \frac{e_p}{e_p + c_p} \quad (3.18)$$

The number of occupied traps in thermal equilibrium can also be determined by the product of the total number of trap states and the occupation probability of the trap state which is given by the Fermi-Dirac distribution

function modified in the case of trap levels by the ratio of degeneracy factors for the unoccupied (g_0) and occupied state (g_1), respectively.

$$\frac{n_t}{N_t} = \frac{1}{1 + \frac{g_0}{g_1} \exp\left(\frac{E_t - E_F}{kT}\right)} \quad (3.19)$$

Combining equations 3.18 and 3.19, one obtains an interesting relation for the ratio of emission and capture rate:

$$e_n = c_n \frac{g_0}{g_1} \exp\left(\frac{E_t - E_F}{kT}\right) \quad (3.20)$$

and

$$e_p = c_p \frac{g_1}{g_0} \exp\left(\frac{E_F - E_t}{kT}\right). \quad (3.21)$$

(The fraction of degeneracy factors g_0/g_1 is often assumed to be about 1.) Equations (3.20) and (3.21) describe how the occupation of a trap state depends on the position of the Fermi level E_F relative to the trap level E_t . This is due to the dependence of the capture rate on the free carrier concentrations as shown in equations 3.9 and 3.10. If the Fermi level is above E_t , c_n is larger than e_n and c_p is smaller than e_p , so that the trap state is occupied by electrons. If otherwise the trap state is above the Fermi level, c_n is smaller than e_n and c_p is larger than e_p and therefore the deep level is unoccupied by electrons. Besides the relation of emission and capture rates for the same type of charge carrier, equations 3.20 and 3.21 are also important to judge the relative magnitudes of electron and hole emission rates of a deep level. If the capture rates are replaced by equations (3.9) and (3.10), the following expression for the number of free charge carriers is obtained:

$$\begin{aligned} n &= N_c \exp\left(-\frac{E_c - E_t}{kT}\right) \\ p &= N_v \exp\left(-\frac{E_t - E_v}{kT}\right), \end{aligned} \quad (3.22)$$

where N_c and N_v are the effective densities of states in the conduction and the valence band, respectively

$$N_{c/v} = 2 \left(\frac{2\pi m_{n/h} kT}{h^2} \right). \quad (3.23)$$

Equations 3.24 and 3.25 give the temperature dependence of the normalized emission rate:

$$e_n(T) = \sigma_n v^{th} N_c \frac{g_0}{g_1} \exp\left(-\frac{E_c - E_t}{kT}\right). \quad (3.24)$$

For a hole trap, the respective equation is:

$$e_p(T) = \underbrace{\sigma_p v^{th} N_v \frac{g_0}{g_1}}_{\nu_0 \text{ resp. } \xi_0 T^2} \exp\left(-\frac{E_t - E_v}{kT}\right). \quad (3.25)$$

For a trap state in the upper half of the band gap, $(E_c - E_t)$ is smaller than $(E_t - E_v)$, therefore, assuming pre-exponential factors of the same order of magnitude, e_n is larger than e_p in this case. For a deep level in the lower half of the band gap, the situation is exactly the opposite and e_p is larger than e_n . This concept to determine the dominant emission rate depending on the relative position of the trap state within the band gap leads to the discrimination between majority carrier traps and minority carrier traps. Majority carriers (minority carriers) are electrons (holes) in an n-type semiconductor or holes (electrons) in a p-type semiconductor. If the emission of majority carriers is dominant, the trap is referred to as majority carrier trap. If the emission of minority carriers is faster, then it is called a minority carrier trap. Moreover equations 3.24 and 3.25 show that the emission of charge carriers from a deep level is a thermally activated process. Assuming a temperature independent, not thermally activated capture cross section, the so called activation energy is given by the distance between the energetic position of the trap level within the band gap and the band edge it corresponds with, i.e., its distance to the conduction band minimum or valence band maximum ($E_a = E_c - E_F$ or $E_a = E_F - E_v$). (If $\sigma_{n/p}$ is also thermally activated, the activation energy is actually the sum of both contributions, the activation energy of the capture cross section and the energetic distance between the trap level and the corresponding energy band.) The pre-exponential factor shows an over-all quadratic temperature dependence, as the effective density of states is given by equation (3.23) and the mean thermal velocity by:

$$v^{th} = \sqrt{\frac{3kT}{m_{n/h}}}. \quad (3.26)$$

Here $m_{n/h}$ is the effective mass for electrons and holes, respectively, and h is Planck's constant. Sometimes, this temperature dependence is neglected as it is weak compared to the exponential dependence. In this case the activation energy of a deep level is obtained from a plot of the logarithm of the emission rate versus inverse temperature and the pre-exponential factor is called ν_0 . Alternatively, if the temperature dependence of the prefactor — which is then referred to as $\xi_0 T^2$ — is taken into account, E_a is determined from a plot of logarithm of emission rate divided by the square of temperature versus the inverse temperature. The capture cross section can also be calculated from

these fits as can be seen from equations (3.24) and (3.25), assuming either a temperature dependent or independent prefactor.

Chapter 4

Experimental Techniques

In the preceding chapter, the space charge region, the impact of deep levels on the depletion region width, capture and emission kinetics and thermally activated emission were introduced. In the following, this information will be used to explain the working principles of the experimental techniques applied within the scope of this thesis. That are admittance spectroscopy (AS) and deep level transient spectroscopy (DLTS). Firstly, an introduction to the experimental techniques is given. Afterwards, some deviations from ideal assumptions made when describing the measurement techniques and their consequences for interpretation of experimental data are discussed, too. At last, the experimental setup used for the respective measurements will be described.

4.1 The a.c. equivalent circuit of Schottky and p-n diodes

For electrical measurements in alternating current mode, p-n junctions and Schottky diodes can be described by a capacitor and a resistor in parallel as equivalent circuit. The resistance stands for all parasitic leakage currents. The capacitance represents the space charge region, which can be approximated by a parallel plate capacitor:

$$C = \frac{\epsilon\epsilon_0 A}{x_d}, \quad (4.1)$$

provided the assumptions of the depletion approximation that was already mentioned in the last paragraph of section 3.1 are met [45]. Here, A is the junction area, x_d is the width and C the capacitance of the space charge region. As the width x_d is determined by the occupation and concentration of electrically active centers present, dopants and deep levels, impedance measurements are appropriate to investigate the levels' properties and concen-

trations. There exist several different techniques which can be divided into experiments with continuous excitation and time resolved measurements after abrupt perturbation of a steady state. The impedance (or its inverse, the admittance) is one of the complex functions describing physical properties, where the real and the imaginary part are directly related by the Kramers-Kronig relation. For an arbitrary complex function

$$f(\omega) = f_1(\omega) + if_2(\omega) \quad (4.2)$$

where f_1 and f_2 are the real and the imaginary part of function f , respectively, the Kramers-Kronig relations are

$$f_1(\omega) = \frac{-2\omega}{\pi} \int_0^\infty \frac{\omega' f_2(\omega')}{\omega'^2 - \omega^2} d\omega' \quad (4.3)$$

and

$$f_2(\omega) = \frac{2\omega}{\pi} \int_0^\infty \frac{f_1(\omega')}{\omega'^2 - \omega^2} d\omega'. \quad (4.4)$$

So, if the real part of the function f is known in the angular frequency range from zero to infinity, the imaginary part can be calculated and vice versa. In fact, both, the real and the imaginary part, actually provide the same information. However, for admittance or impedance measurements, experiments with continuous excitations and time resolved techniques, it has become customary to evaluate the capacitance data.

4.2 Admittance spectroscopy

Measuring the admittance $Y = G + i\omega C$ as a function of the angular frequency ω ($\omega = 2\pi f$) of the applied alternating voltage is a technique to investigate deep levels in semiconductor devices using continuous excitation. A sinusoidal voltage of small amplitude is applied to the sample and the resulting current is detected phase sensitively. During measurement, a frequency sweep is performed. The frequency dependent admittance $Y(\omega)$ is obtained by division of the resulting current by the excitation voltage. The physical processes occurring can be described as follows. The periodic potential applied induces an alternating shift of the Fermi level E_F or quasi-Fermi level of the majority carriers E_{Fn} or E_{Fp} . This movement leads to a continuous change in charge $\delta q_d(t)$ which is in phase with the excitation voltage and leads to a decrease and increase in depletion width. If deep levels are present, that are crossed by the Fermi level, the intersection point of trap level E_t with E_{Fn} (or E_{Fp}) is shifted, too, so that in vicinity of the point of intersection, the occupation of trap levels changes continuously and leads to an additional trap induced change in charge $\delta q_t(t)$. So the resulting current can be described by:

$$i(t) = \frac{d}{dt}\delta q_d(t) + \frac{d}{dt}\delta q_t(t), \quad (4.5)$$

where it has to be noted, that $\delta q_d(t)$ and $\delta q_t(t)$ are not independent. From equation 4.5 we can now see, how the frequency dependence of Y comes about. Firstly, a trap free device shall be considered. Here the alternating voltage induces a change in charge of the depletion width $\delta q_d(t)$ which is in phase with the excitation. The resulting current which is the time derivative of $\delta q_d(t)$ is therefore $\pi/2$ in advance of $v(t)$ behaving like a lossless capacitor. The capacitive contribution of the space charge region is only absent at small temperatures, when the free carrier freeze out leads to a depletion region which spans the whole semiconductor device from one contact to the other. The semiconductor layer(s) then behave(s) like a dielectric in between two parallel plates. The measured capacitance is called geometric capacitance as it is inversely proportional to the thickness of the device.

If now deep levels are present in the device, there can be another current contribution in addition to the depletion capacitance coming from reloading of the trap states, as mentioned earlier. The capture and emission of charge carriers into and from deep levels, respectively, is not infinitely fast. Moreover, as occupational changes occur only where E_t crosses E_F , the capture and emission rate are approximately equal (see equation (3.20) and (3.21)). One has to consider two different scenarios. At low frequencies reloading of deep traps leads to a change in charge δq_t which is in-phase with $v(t)$ and therefore produces an imaginary contribution in addition to the depletion capacitance. When the measurement frequency is enlarged, the traps cannot respond instantaneously anymore and δq_t lags behind $v(t)$. This means that the leading angle of the current is now less than $\pi/2$ which produces a real component of $i(t)$ and reduces the imaginary contribution of the traps. If the frequency is that high that the phase shift between δq_t and $v(t)$ is $\pi/2$, then only a real component is produced by the traps and the imaginary part consists exclusively of the depletion capacitance. The respective equation giving the frequency dependent capacitance per unit area is:

$$C'(\omega) = \frac{\epsilon\epsilon_0}{x_d} + \left(1 + \frac{\omega^2}{f_t^2}\right)^{-1} \Delta C' \quad (4.6)$$

with

$$f_t = 2e_n \left(1 + \frac{x_t N_t}{x_d N_d}\right) \quad (4.7)$$

and

$$\Delta C' = \frac{\epsilon\epsilon_0 N_t}{x_d N_d} \left(\frac{1 - x_t/x_d}{1 + (x_t N_t)/(x_d N_d)}\right) \quad (4.8)$$

The first term of the sum is the depletion capacitance, the second the contribution of a deep level. (In the case of a p-type semiconductor e_n has to

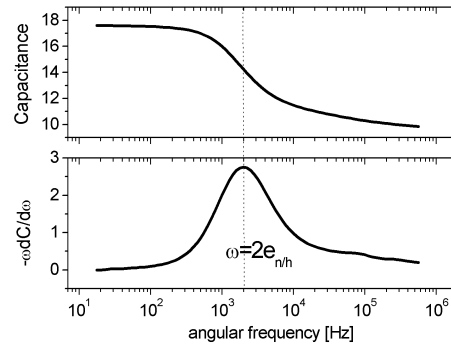


Figure 4.1: Schematic of a capacitance versus angular frequency (top) and $-\omega dC/d\omega$ versus angular frequency diagram (bottom), respectively. The inflection point in the C vs ω graph corresponds to the maximum in the $-\omega dC/d\omega$ vs. ω graph and represents the angular frequency that is about equal to 2 times the emission rate of the trap state investigated.

be replaced by e_p and N_d by N_a .) The symbol x_t is the mean depth where occupational changes at the trap state takes place. The frequency dependent capacitance is drawn in figure 4.1. At half height of the capacitance step $\Delta C'$ due to the trap contribution, the angular frequency ω equals f_t . For clarity, it became customary to plot $-\omega \frac{dC}{d\omega}$ versus ω instead of C' . This expression shows a maximum at $\omega = f_t$, and the angular frequency of interest can be easily determined. If one or both of the ratios x_t/x_d and N_t/N_d is/are small, then f_t equals $2e_n$, otherwise f_t is a little larger (The respective conditions hold for a p-type semiconductor, too). The same condition ($x_t \ll x_d$ and/or $N_t \ll N_d$) also facilitates the expression for $\Delta C'$ in equation (4.8). The height of the capacitance step due to deep level contribution is then approximately equal the factor in front of the bracket term. From admittance measurements at different temperatures, the activation energy and capture cross section of the deep level can be determined as described in section 3.5. Here again, it should be emphasized that only deep levels whose energy level E_t exhibits an intersection point with the Fermi level can be detected. In general, these are majority carrier traps, e.g., electron traps in an n-type and hole traps in a p-type semiconductor, but interface defects, that usually span a wide energy range, too. The admittance spectroscopy is suitable to study "shallower" trap levels, as the frequencies applied range typically from 100 Hz to 1 MHz for handling purposes. This will become more clear in the next section, where the deep level transient spectroscopy is discussed, which is more suitable for deeper traps.

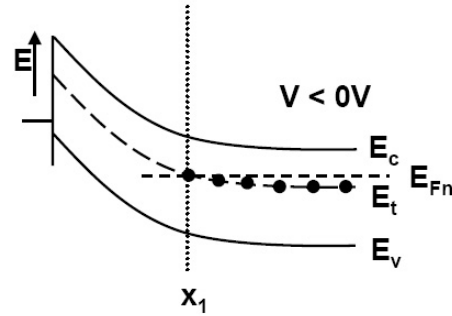


Figure 4.2: First phase of the DLTS measurement sequence shown for a band diagram (energy vs. distance representation) of a metal/n-type semiconductor Schottky diode. Traps states that are energetically positioned above the Fermi level are unoccupied, those below E_{Fn} are occupied by electrons. x_1 marks the position, where E_t equals E_{Fn} .

4.3 Deep level transient spectroscopy (DLTS)

This technique to investigate the properties of trap states is actually a time resolved measurement of the depletion region admittance at a fixed frequency. To ensure exclusively the measurement of the space charge capacitance (no trap response!), f has to be appropriately high, typically 1 MHz. After the description of the measurement principle and the physical process occurring thereby, the evaluation procedure of experimental data will be discussed. Afterwards some deviations from ideal assumptions and their impact on data appearance and interpretation will be mentioned.

4.3.1 General principle: majority carrier DLTS

In the following, a detailed description of the physical processes occurring during experiment will be given, yet, restricted to capacitance transients [75]. A measurement can be divided into three different parts. These are illustrated in figures 4.2, 4.3 and 4.4 for a metal n-type semiconductor Schottky diode with a single (or point-like) majority carrier defect level, i.e., an electron trap. Although the physical processes are discussed for a space charge region extending into an n-type semiconductor, the equations given are also valid for a respective p-type material. Exceptions will be indicated when occurring. For clarity, the density of traps occupied by electrons n_t can be replaced by $N_t - p_t$ to obtain expressions for the number of traps occupied by holes.

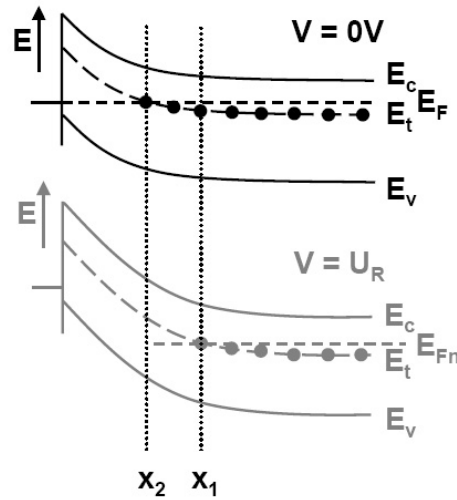


Figure 4.3: Upper dark diagram: Second phase of the DLTS measurement sequence shown for a band diagram (energy vs. distance representation) of a metal/n-type semiconductor Schottky diode. The filling of empty trap states that are positioned energetically below the Fermi level E_F . x_2 indicates the intersection point between E_t and E_F . The light gray diagram below shows again phase one for direct comparison of the positions of the intersection points x_1 and x_2 and the space charge widths at different bias.

In the first phase, the device is held under quiescent reverse bias. The trap level is occupied by electrons up to the intersection point between the trap level E_t and the quasi-Fermi level for majority carriers, e.g., in this example electrons E_{Fn} (see figure 4.2).

In the second part, a voltage pulse is applied to the device under test which reduces the negative bias at the device. Because of the reduced potential difference, the quasi-Fermi level of majority carriers moves upward and the position, where E_t equals E_{Fn} , is now closer to the metal-semiconductor interface as shown in figure 4.3. The trap states between x_1 and x_2 become occupied by electrons. The capture of majority carriers to the trap states is ensured by reducing the reverse bias at maximum to 0 V. This is the characteristics of majority carrier DLTS: Under this condition, basically no minority carriers are injected by the pulse and only majority carriers are available for capture. The situation with minority carriers present during voltage pulse application will be discussed in the next section. As can be seen from equations (3.7) and (4.1), the reduced potential difference during application of the voltage pulse, the width of the space charge region is decreased and its

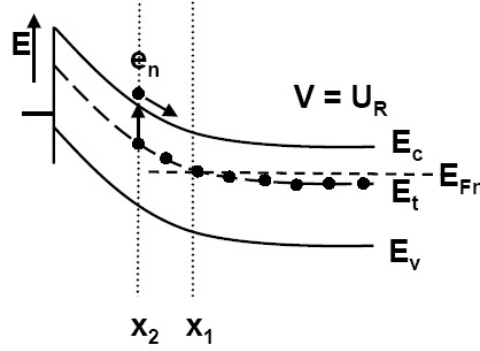


Figure 4.4: Third phase of the DLTS measurement sequence shown for a band diagram (energy vs. distance representation) of a metal/n-type semiconductor Schottky diode. The electrons from trap states that are now above the quasi-Fermi level E_{Fn} , i.e., between x_2 and x_1 , experience thermally activated emission.

capacitance is increased.

The third and last part of the experiment is the situation after application of the voltage pulse which is demonstrated in figure 4.4. Now the sample is under reverse bias again and the depletion region expands again due to the increased potential difference applied. The intersection point between E_t and E_{Fn} has moved further away from the interface (x_1). However, the electrons (majority carriers) in the trap states between x_2 and x_1 cannot instantaneously be emitted due to the thermal activation of this process as shown in equations 3.24 and 3.25. Because of these electrons, the net positive charge in the space charge region (as we deal with an n-type semiconductor; in a metal p-type semiconductor the space charge is net negative) is reduced compared to the equilibrium situation, i.e., the situation before application of the voltage pulse. This means, that the depletion region directly after the voltage pulse is larger and its capacitance is smaller than in thermal equilibrium. (This is also the reason for, why x_1 after application of the voltage pulse is larger than x_1 before its application.) Then, the electrons are bit by bit emitted from the deep states between x_2 and x_1 . This leads to a decrease in depletion region width down to its equilibrium value and an increase of the depletion capacitance increases, respectively. The relaxation process can be described by the time dependent change in net positive space charge $\rho(x, t)$, which is

$$\rho(x, t) = q \left[\underbrace{N_d(x) - N_a(x)}_{N^+} + (N_t(x) - n_t(x, t)) \right] \quad (4.9)$$

for a donor-like trap, i.e., a deep level, that is neutral when occupied by electrons. (For an acceptor-like trap, the expression $N_t(x) - n_t(x, t)$ has to be replaced by $-n_t(x, t)$.)

Using Poissons equation (3.6), the relation

$$dV = \frac{q}{\epsilon\epsilon_0} \left(x_d N^+(x) dx_d + [N_t - n_t(t)] x_1 dx_1 - \frac{1}{2} [x_1^2 - x_2^2] dn_t \right). \quad (4.10)$$

is obtained. In the case of capacitance transient observation which shall be considered here the potential difference is kept constant during observation of the thermal emission of charge carriers ($dV = 0$). Differentiating equation (4.10) and setting it equal to zero gives at last the following expression for the capacitance transient:

$$\Delta C(t) = \Delta C_0 \exp(-t/\tau) \quad (4.11)$$

where

$$\frac{\Delta C_0}{C} = -\frac{1}{2} \left\{ \frac{x_1^2 - x_2^2}{x_d^2} \right\} \frac{n_t(0) - n_t(\infty)}{N^+} \quad (4.12)$$

Here, the relations $dC/C = -dx_d/x_d$, $dC = \Delta C(t)$ and $dn_t = \Delta n_t(t)$ have been used in conjunction with some other simplifications valid for small trap concentrations $N_t \ll N^+$. Also, equation 3.14 has been inserted to express $n_t(t)$. The capacitance transient is an exponential decay where the time constant τ is the sum of all capture and emission rates (see equation (3.16)). $n_t(\infty)$ is the number of occupied traps under steady state conditions, which is usually $n_t(\infty) = 0$ and (equation (3.15)) and $n_t(0)$ is the initial number of occupied traps given by equation (3.14), where the time is the duration of the voltage pulse. The capacitance transient of the trap filling during application of the voltage pulse can be described by equation (4.11) as well, inserting $n_t(0) = 0$ and $n_t(\infty)$ as given by equation (3.15). A closer look at the time constant τ shows, that for the occupation kinetics of a majority carrier electron trap within positions x_2 and x_1 of the depletion region (figure 4.4), actually not all capture and emission rates play a role in the specific example. Referring to section 3.5, the deep level can be identified as majority carrier trap in an n-type semiconductor, so $e_n > e_p$. Moreover the capture of holes can be neglected, too, as the minority carrier concentration within the depletion region is about zero under measurement conditions. Considering now the fact that between x_2 and x_1 , the trap level E_t is above the quasi-Fermi level, it becomes clear that c_n is smaller than e_n . So all in all, τ is approximately equal to e_n . For a majority carrier trap, where the space charge region extends into a p-type semiconductor, e_p is the dominant process. The activation energy of a majority carrier trap can be obtained

from temperature dependent determination of the inverse time constant of the capacitance transients as described by equations (3.24) and (3.25).

Some additional comments have to be made. Comparing the situation at $t = 0$ and $t = \infty$, it can be seen, that $n_t(0) > n_t(\infty)$ and $x_2 < x_1$. Considering equation (4.12), this means, that $\Delta C_0/C$, the amplitude of the capacitance transient (normalized to the equilibrium capacitance) is negative. This result is quite important as the negative sign is characteristic of majority carrier defect transients. This will be discussed again in the next section after introduction to investigation of minority carrier defects.

Another aspect is the deep level concentration: N_t can be calculated from the initial amplitude of the capacitance transient normalized to the equilibrium capacitance as given by equation 4.12 provided the doping concentration is known and the deep level concentration is small compared to N^+ . Under certain conditions, assuming $x_2 < x_1$, $n_t(0) = N_t$ and $n_t(\infty)$, equation 4.12 reduces to:

$$\frac{\Delta C_0}{C} = \frac{N_t}{2N^+}. \quad (4.13)$$

At last, the spacial sensitivity of capacitance DLTS shall be mentioned. Assuming a constant doping and deep level concentration, the normalized change in capacitance at position x is [76]:

$$\left\{ \frac{\Delta C}{C} \right\}_x = -\frac{n(x)}{N^+ x_d^2} x \Delta x. \quad (4.14)$$

So $\Delta C/C$ increases linearly with position within the space charge region, where $x = 0$ is located at the junction interface. From this expression it can be seen, that capacitance DLTS is a bulk sensitive measurement technique [77, 76]. Interface defects are only detected under special conditions.

4.3.2 Minority carrier DLTS

As shown in the preceding section, the DLTS experiment can be conducted in such a way that only majority carrier traps are affected by perturbation from steady state. As deep levels of minority carriers — in contrast to majority carrier deep levels — exhibit no intersection point with the (quasi-)Fermi level at reverse or zero bias voltage, the experiment has to be performed a little different. The sample is again held under reverse bias. Then, a voltage pulse is applied, but this time it drives the device into forward direction so that minority carriers are injected. For duration of the pulse, the quasi-Fermi level of minority carriers lies completely below E_t . The minority carrier trap level experiences therefore a fast capture of minority carriers as shown in figure 4.5.

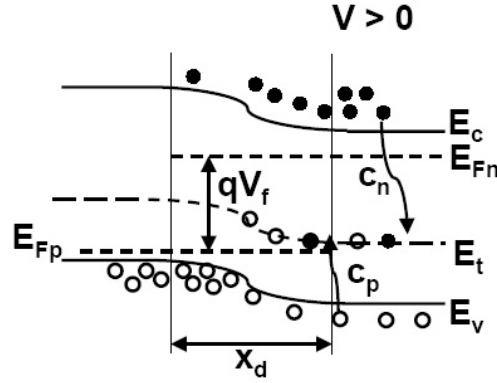


Figure 4.5: Band diagram (energy vs. distance representation) of a p-n junction. The Situation during application of the voltage pulse in minority carrier DLTS is shown. The traps states above the minority carrier quasi-Fermi level become filled with minority charge carriers. However, as majority carriers are present, too, there's a competition between the two types of charge carriers about occupation of the deep levels.

At last, after application of the voltage pulse, the device is again under reverse bias and relaxes to equilibrium. Immediately, the depletion region width is adjusted to the respective potential difference applied. However, the charge carriers trapped in the minority carrier deep level cannot respond instantaneously. Within the space charge region, the minority carrier traps are, similar to the majority carrier DLTS experiment, emptied from minority carriers by thermal emission. However, at the edge of the depletion region, the minority carriers vanish by capture of majority carriers. The minority charge carriers initially captured within the trap levels after application of the voltage pulse increase the net positive or negative space charge of the depletion region. The width of the depletion region is therewith initially decreased and its capacitance increased, respectively, compared to the equilibrium situation. The emission of minority carriers leads therefore to a capacitance transient with positive amplitude. The analytic equation describing this process, can be obtained from equations (4.11) and (4.12), if one considers, that minority carriers are emitted from the region $x_1 = x_d - \lambda$, which is the edge of the depletion region minus the small transition region λ , where the free carrier density falls down to zero, to $x_2 = 0$, which is the actual interface between p- and n-side of the junction. One also has to take into account that in equilibrium, the minority carrier trap is fully unoccupied by minority carriers ($N_t - p_t(\infty) = N_t$). The initial occupation $p_t(0)$ can be calculated again from equation (3.14). With these slight modifications, the

capacitance transient of minority carrier emission expressed in terms of a hole trap is given by:

$$\Delta C(t) = \Delta C_0 \exp(-e_p t) \quad (4.15)$$

with

$$\frac{\Delta C_0}{C} = \frac{1}{2} \left\{ 1 - \frac{\lambda}{x_d} \right\}^2 \frac{p_t(0)}{N^+}. \quad (4.16)$$

For an electron minority carrier trap, e_p is replaced by e_n and $p_t(0)$ by $n_t(0)$. As expressed in equations (4.11) and (4.15), the amplitude of the capacitance transient has a positive sign for minority carrier emission and a negative one, if majority carriers are emitted. Therefore this measurement technique is capable to determine which type of charge carrier is captured/emitted into/from a specific trap level.

Some additional remarks have to be made to the minority carrier DLTS experiment. In contrast to majority carrier DLTS, this technique is not specific to minority carriers. Actually minority carrier traps and majority carrier deep levels do likewise respond to this kind of perturbation. This has to be taken into account in data interpretation and therefore will be discussed in more detail in section 4.3.4. Another aspect is that the voltage pulse in forward direction is only one opportunity to detect minority carriers. Light pulses with wavelength smaller or larger than the band gap of the semiconductor material can be used as well to perturb the occupation of a minority carrier trap. As this technique was not extensively applied within this thesis, it shall be referred to the detailed information given in the book from Blood and Orton [74].

4.3.3 Reverse bias DLTS (RDLTS)

The reverse bias DLTS method is actually the opposite of the measurement procedure discussed so far: the capture of charge carriers is monitored instead of the emission process. The experiment sequence can be described as follows: as starting point, the sample is held at a low level of reverse bias voltage or at zero bias. The traps up to the intersection point x_2 between the majority carrier trap level and the Fermi level are occupied by electrons (majority carriers). Then, a voltage pulse is applied but this time it drives the device in reverse bias direction, so that the intersection point, now called x_1 , moves further away from the metal-semiconductor interface and the defect levels between x_2 and x_1 empty by thermal emission of majority carriers. After application of the voltage pulse, the sample is under low bias voltage or zero bias again and the intersection point, now again named x_2 moves closer to the interface. The defect levels unoccupied (by majority) carriers in between x_1 and the new x_2 are refilled by capture of majority carriers. (Note that

in accordance with the description of majority and minority carrier DLTS, the intersection point under low reverse bias voltage (respectively zero or forward bias) is called x_2 , whereas it is named x_1 under comparatively large reverse bias.) The trap occupation can be calculated from equation (3.14) with $n_t(\infty) \approx N_t$, and $\tau = c_n$ for an electron majority carrier trap level in an n-type semiconductor. The density of occupied traps initially after application of the voltage pulse depends on the pulse duration t_p :

$$n_t(0) = N_t \exp(-e_n t_p). \quad (4.17)$$

The time dependence of the number of occupied traps after application of the voltage pulse is then:

$$n_t(t) = N_t - N_t \{1 - \exp(-e_n t_p)\} \exp[-c_n(x)t]. \quad (4.18)$$

This filling process is monitored as capacitance transient. As can be seen from equation (4.12), $\Delta C_0/C > 0$, when majority carriers are captured, taking into account that $n_t(0) < n_t(\infty)$ and considering that $x_1 > x_2$. Per theoretical considerations from Li and Wang [78, 79], the capture at the intersection point, where the respective capture rate equals the emission rate (see section 3.5), dominates the inverse time constant of the capacitance transient. Therefore the inverse time constant is equal to the thermal emission rate of the captured charge carriers, so that this technique under these assumptions is capable to determine the activation energy of a deep level as well. The authors also indicate a higher spatial resolution which makes the method appropriate for concentration profiling, too.

4.3.4 Evaluation with a weighting function

After the actual DLTS measurement, majority carrier, minority carrier DLTS or reverse bias DLTS, the obtained capacitance transients for different temperatures have to be evaluated in terms of determination of the temperature dependent emission rates. As one deals with data that corresponding to equations (4.11) and (4.15) show exponential behavior, a simple exponential fit should be enough to determine the parameters of interest (initial amplitude and emission or capture rate). However, in real samples it can happen that the capacitance transient is a sum of signals from several different traps. So, a more general ansatz like the inverse Laplace transform appears more appropriate [80, 81]. There actually exist several algorithms and full programs for this task [82]. However, there are several constraints that have to be considered and are experimentally sometimes not very easy to meet. For example, the transients have to be recorded until complete decay, which can be sometimes very time consuming [81]. Then, the data points sometimes have to be equally spaced [83], which — especially if the first constraint shall

be fulfilled — requires storage of large amounts of data. Constant offsets can also be problematic, and they can not completely be prohibited in a real experiment. Another important constraint is that the capacitance transient can only be evaluated, if the transients that contribute to the measured capacitance signal have the same sign [82]. One might now say that at least for majority carrier DLTS measurements, this should be no problem, but as real samples are often not ideal, this condition can not always be met. In short, elaborate high resolution evaluation procedures are also more susceptible to errors. So, a quite old but also quite stable procedure was chosen.

The data evaluation with help of a so called weighting function has been used since the beginning of DLTS investigations [75]. As the concept could be applied already during the actual measurement, only the result of the evaluation had to be stored on a computer and not the whole capacitance transient, which at this time was an important reduction of disk space consumption. The principle can be described as follows. The capacitance transient obtained from experiment is multiplied by a correlation function, integrated over the period of this function and normalized to it. There exist many different weighting functions with different resolution, called filter orders, and signal to noise ratios (S/N) [84]. Within this thesis, the "double boxcar weighting function with optimized time delay t_d " was applied as appropriate compromise between resolution and (S/N) ratio. In this case, the evaluated DLTS signal is obtained as:

$$S(T, t_c) = t_c^{-1} \int_{t_d}^{t_d+0.1t_c} \frac{\Delta C(t)}{C} dt - \int_{t_d+0.9t_c}^{t_d+t_c} \frac{\Delta C(t)}{C} dt. \quad (4.19)$$

The procedure is repeated for different periods t_c . The result of this evaluation is visualized in figure 4.6. The DLTS signal $S(T, t_c)$ basically gives in principle the difference in transient values for two small time windows. The signal is maximum when the transient decays almost completely during t_c . The delay t_d between the end of the voltage pulse ($t = 0$) and the beginning of the transient evaluation provides a better resolution. For the double boxcar function it should be chosen such that $t_d/t_c = 0.131$. The maximum in the $S(T, t_c)$ versus temperature graph indicates the temperature, where the inverse time constant of the charge carriers emitted from the specific trap level is proportional to t_c ($\tau_{max}^{-1} = e_{n/p} = 1.996t_c$). These temperature dependent emission rates obtained from $S(T)$ vs. T graphs of different periods of the weighting function are then utilized to build an Arrhenius diagram as described in section 3.5. The sign of the capacitance transients evaluated is retained: majority carrier trap signals give a negative peak, minority carrier deep levels a positive one. The peak amplitude is also proportional to the one of the capacitance transient ($S(T) = 0.058(\Delta C/C)$), so that the deep level concentration can be calculated using equation 4.13, too. The DLTS peaks

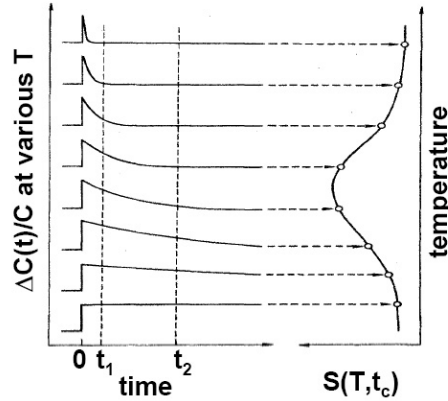


Figure 4.6: Presentation of the evaluation process of capacitance transients at different temperatures using the double boxcar weighting function. The time intervals t_1 and t_2 are assumed infinitely small. (The schematic is taken from Lang et al. [75] with slight modifications.)

in these spectra have a defined broadness. The full width at half height of the maximum or minimum is for the double boxcar function with optimized time delay:

$$\frac{\Delta T}{T} = \frac{\ln(16.5)}{2 + E_a/(kT)} \quad (4.20)$$

where E_a is $(E_c - E_t)$ and $(E_t - E_v)$, respectively. For most traps, $\Delta T/T$ is about 0.1.

One additional remark has to be made concerning the evaluation of minority carrier DLTS experiments. As already mentioned in the previous section, this specific experimental technique can detect majority and minority carrier traps. This means for the respective DLTS signal versus temperature spectra, that they are actually a sum of majority carrier and minority carrier response. So, to extract the pure minority carrier spectrum, the majority carrier spectrum actually has to be subtracted from it. However, in practice, it is not very easy to determine the initial number of traps occupied by minority carriers as this depends on minority and majority carrier rates (see equations (3.14)). This means that not necessarily all traps become occupied even for long enough duration of the voltage pulses and quantitative results can be considered only as good guesses.

4.3.5 Non-exponential transients

For the derivation of the analytic equations describing the thermally stimulated emission of charge carriers in a DLTS experiment, a single defect level with a defined emission rate was assumed. However, experimental data do often deviate from a mono-exponential decay. In the DLTS signal versus temperature graphs, this kind of transients leads to broadened peaks which have a width larger than approximately 0.1 (see equation (4.20)). There are many fold attempts to explain this behavior. In the following, some of them should be addressed.

Large trap concentrations

As already indicated in section 4.3.1, equations (4.11) and (4.15) are only valid for small trap concentrations. If this is not the case, the capacitance transient is non-exponential until the density of charge carriers that are about to be emitted from the trap level becomes small (as a lot of charge carriers have already been emitted), so that $N_t \ll N^+$ is valid again. (In contrast to that, voltage transients which are obtained keeping the depletion capacitance constant show exponential behavior irrespective of the deep level concentration.) This seems to cause some problems concerning the data evaluation, because the method to utilize a weighting function to determine the inverse time constant of a capacitance transient was originally developed only for data with exponential behavior. However, Cohen and Lang [85] showed, that even for $N_t \approx N^+$, the evaluation of transients using the boxcar weighting function is an appropriate procedure to determine the trap parameters. Concerning the trap concentrations, the correct order of magnitude is obtained utilizing equation 4.13.

Alloy broadening

If the semiconductor material is an alloy for instance of two components A and B, the local composition is not the same throughout the material but shows slight compositional variations. These fluctuations lead to locally varying activation energies of the occurring defects. Omling et al. [86] investigated this phenomenon for $\text{GaAs}_{1-x}\text{P}_x$ and assumed a Gaussian distribution for the activation energies of the trap levels.

$$C(t) = \int_0^\infty g(E_{ai})C_0 \exp[-e_{n/p}(E_{ai})t]dE_{ai} \quad (4.21)$$

with

$$g(E_{ai}) = \frac{1}{\sigma\sqrt{2\pi}} \exp\left(\frac{-(E_{ai} - E_{a0})^2}{2\sigma^2}\right). \quad (4.22)$$

E_{ai} is the activation energy varied from zero to ∞ , and σ is the standard deviation and gives a measure of the alloy broadening. Within their model, they calculated DLTS signal versus temperature spectra for different broadening levels σ ($\sigma = 0$ corresponds to a mono-exponential decay) and found, that irrespective of σ , the peak position stays at the same temperature and the area under the signal is constant, too. However, the signal amplitude is reduced due to signal broadening ($\Delta T/T > 0.1$). For the determination of deep level activation energies this means, that even under these conditions, the evaluation of the transient using a weighting function gives the characteristic trap parameters, which are in this case the mean values for the respective deep level distribution.

Arbitrary distribution of defects

The Gaussian distribution of deep level activation energies found in the case of alloy broadening is actually a quite specific case. One can also imagine an arbitrary distribution of defect states to be present within the band gap, for instance induced by dislocations [87]. However, even under these conditions, the analysis of capacitance transients (although they are non-exponential) using a weighting function give correct results. Cohen and Lang were again able to demonstrate, that the DLTS versus temperature spectrum is formally to a certain extend the Laplace transform of the original capacitance transients [85]. So, not only Gaussian but arbitrary distributions of defect states are correctly reproduced by this evaluation scheme.

Capture in the Debye tail

Within the depletion region, usually the free carrier density is assumed to be zero and the free carrier concentration is considered to fall exponentially off to zero when approaching the edge of the depletion region from the bulk, which is called the "Debye tail" or "transition region". However, the transition from bulk carrier concentration to zero can be considered as quasi abrupt only, when the difference in bias levels during and after application of the voltage pulse is sufficiently large, so that the majority of traps that change occupation during the measurement sequence is located within the depletion region at reverse bias and in the neutral region during pulse application, respectively. Otherwise the non-zero free carrier concentration within the transition region causes a modification of the inverse time constant of the capacitance transient. As can be seen from equation (3.16), τ^{-1} is in general the sum of all capture and emission rates possible. Only under certain conditions, it can be approximated by e_n and e_p respectively (see section 4.3.1). In

case of a non-negligible free carrier concentration in the space charge region, τ^{-1} is the sum of the capture and emission rate of the respective type of charge carrier. As the capture rate is directly proportional to the free carrier concentration, the resulting inverse time constant shows a respective spacial variation and the measured capacitance transient is a sum of exponential decays with different inverse time constants [88, 89]. The capture rate is at maximum at the depletion region edge. The influence of the capture process on the inverse time constant can be seen from a variation of the height of the voltage pulse applied: the larger the amplitude of the excitation pulse (fixed level of reverse bias), the lower is its influence on τ^{-1} and therewith the absolute value of the inverse time constant. For the DLTS versus temperature diagram this means a shift of the DLTS peak to lower temperatures, i.e., smaller activation energies, with increasing height of voltage pulse, if capture in the Debye tail occurs. A non-negligible capture rate can also be recognized by a dependence of the signal amplitude $\Delta C(0)/C$ on the reverse bias applied to the device, while keeping the height of the voltage pulse fixed as shown in reference [88]. An influence of the capture rate can also occur, when the diode leakage current is non-negligible and therefore the free carrier concentration is larger than zero in the depletion region [90].

Electric field enhanced emission

The emission rate of a deep level can also be influenced by the potential difference present over the width of the space charge region extending from its maximum value at the junction to zero at the edge of the depletion region. Because of the variation in electric field over the depletion region the emission rate becomes spatially dependent and the resulting capacitance transient is therefore a sum of exponential decays with different inverse time constants. This influence is called "electric field effect on thermal emission" [91]. The actual mechanisms can be divided into three groups: lowering of the potential wall, wherein the charge carrier is trapped if it occupies a deep level (the Poole-Frenkel effect), phonon-assisted tunneling and the pure tunneling effect. In addition to that, the actual form of the potential well, either more Coulomb-like or Dirac-like well, does play a role, too. A detailed description of this topic is given in [91]. For deep levels in CIGS, it was stated that phonon-assisted tunneling is the dominant process [92]. To reduce the electric field effect on the emission rate, it is recommended to use only low voltage pulses, as then thermal emission only happens further away from the junction interface, where its influence is only small and about constant due to the small area of observation. The influence of the electric field on the emission rate can be determined by application of different heights of voltage pulse keeping the reverse bias level fixed. An enhancement of the inverse time constant with increasing pulse height, i.e., a shift of the DLTS peak

towards higher temperatures or larger activation energies, is characteristic for this effect.

4.3.6 Devices with non-negligible series resistance

As indicated already in section 4.1, a capacitor connected in parallel to a resistor is assumed as equivalent circuit for the capacitance measurements introduced. However, if the series resistance, e.g., the resistance of the neutral bulk of the device, cannot be neglected for instance because of a low mobility or small free carrier concentration, especially DLTS measurements can be problematic, because the assumption of a wrong equivalent circuit can lead to inversion of the measured DLTS signal and therefore to a wrong assignment in terms of majority or minority carrier trap. If one compares the diode-resistance series circuit ($C_s - R_s$) representation of a device to the diode parallel circuit ($C_p - R_p$) representation, the variations δC_s and δC_p coincide, when $R_s = 0$ or $R_p = \infty$. However, if this is not the case, δC_p and δC_s are related to each other in the following way:

$$\frac{\delta C_p}{\delta C_s} = \frac{1 - Q^2}{(1 + Q^2)^2}, \quad (4.23)$$

where Q is called "quality factor" [93] and is given by

$$Q = \omega R_s C_s. \quad (4.24)$$

Here, ω is the measurement frequency of the capacitance, R_s and C_s are the series resistance and capacitance of the device, respectively. The quality factor serves as a measure, whether the assumed equivalent circuit is appropriate or not. As long as $Q < 1$, the sign of the measured capacitance transient is correct, but the amplitude of the signal might already be reduced. At $Q = 1$, the DLTS signal is canceled and for $Q > 1$, the sign of the signal is inverted, so that negative majority carrier signals appear as positive minority carrier traps and vice versa. In practice, there are two options to check whether a DLTS signal is inverted or not. The first one is the variation of the measurement frequency. As can be seen from equation (4.24), the higher the angular frequency, the larger is Q . So when a DLTS signal changes its direction upon increasing the measurement frequency, the sign obtained at lower frequency is correct. If the signal direction cannot be changed, then it has to be already inverted. Another option, which is often more practical, as capacitance meters usually work at one fixed frequency, is the addition of a series resistance. The identification of the sign inversion is the same as

described before. If no sign change can be induced by an additional R_s , then the signal was already inverted before.

A third option is the evaluation of the time dependent conductance which is automatically measured in every experiment, too, instead of the capacitance. In contrast to capacitance transients, conductance transients do not show any sign inversion even if the $R_s - C_s$ equivalent circuit is more appropriate to describe the device under test than the actually applied parallel equivalent circuit [94]. The transients can be analyzed exactly like the capacitance transients using a weighting function to determine the trap parameters of a deep level from a conductance DLTS (GDLTS) versus temperature diagram. However, the calculation of defect concentrations from the measured signal amplitudes is not that straightforward as for capacitance transients [94].

4.3.7 Minority carrier defect signals in majority carrier DLTS

The precise separation of majority carrier defects and the sum of minority and majority carrier response by different measurement techniques, i.e., non-injecting and injection voltage pulse, is sometimes confused by leakage currents. Minority carriers spilling over the potential barrier of a Schottky barrier, for example, can be trapped in minority carrier defect levels and can give rise to a minority carrier emission even under non-injection conditions. This phenomenon was, for example, observed for a n-type silicon/gold Schottky barrier [95]. Minority carrier defect signals in majority carrier DLTS can also be caused by interface defects or a trap level close to the interface with large concentration or a band of defect states, provided the quasi-Fermi level crosses the trap levels or is close to them so that their occupation becomes voltage dependent even on application of a reverse bias voltage [96].

4.4 Compensation law or Meyer-Neldel rule

The compensation law is a phenomenological relationship found in many thermally activated processes like diffusion in crystals, electrical conduction in amorphous semiconductors [97] and also for thermally stimulated emission of charge carriers from trap states [98]. The rule is often called Meyer-Neldel rule after Meyer and Neldel [99] who found this behavior for activation of electric conduction of oxide semiconductors. The rule says that for a process X_0 that can be described by

$$X = X_0 \exp \{ -E_a / (kT) \} \quad (4.25)$$

the preexponential factor X_0 and the activation energy E_a are connected by the following linear equation

$$\ln(X_0) = a + bE_a. \quad (4.26)$$

There are different Ansätze in literature to explain the origin of this relation. Yelon and Movaghar [100] stated that the rule is obeyed by processes that require large energies compared to the mechanism that provides the excitation energy. The prefactor X is assumed to be "proportional to the number of ways to assemble these excitations" [100]. In case of carrier emission, for example, this could be excitation by phonons. For different sets of defect parameters $E_a - \nu_0$ (for a definition, see section 3.5), the obeyment of the Meyer-Neldel rule is taken as indication of a common origin, i.e., that despite the different activation energies and prefactors one deals with the same kind of trap level. (E_a is then $E_c - E_t$ and $E_v - E_t$, respectively.)

4.5 The experimental setup

The discussion of the experimental techniques shall now be completed by a short description of the experimental setup used. For all measurements, the device under test was mounted in a cryostat. The temperature control was accomplished by a "Lakeshore 340" temperature controller in conjunction with a closed-cycle helium cooling system. The sample is connected to the respective measurement instrument via BNC cables. The actual measurements are conducted from a PC by respective Labview measurement programs. The data are stored on the computer, too. For admittance spectroscopy, two different Impedance Gain/Phase Analyzers (Solatron 1260 and Hewlett Packard 4914A) are utilized. These instruments serve as both, excitation source, i.e., they apply a sinusoidal voltage of adjustable amplitude to the sample, and as analyzers, i.e., they concurrently measure the resulting current in a phase sensitive way. The setup for the DLTS investigations is a little more complex. The heart of the setup is a Boonton 7200 capacitance bridge that measures the time dependent changes in capacitance and conductance by application of a sinusoidal voltage of small amplitude and high frequency. To allow for operation in a more sensitive measuring range, the equilibrium capacitance and conductance are balanced by a home built capacitance and conductance offset instrument. The voltage pulse that has to be applied to the device under test is produced by an Agilent 81104A Pulse Generator. The analog capacitance and conductance data are transformed into digital form by an ADwin Gold A/D converter and transferred to the PC. A detailed description of the DLTS setup can be found in [101].

Chapter 5

Experimental Results

In the following a detailed description of the results obtained from admittance and deep level transient spectroscopy on copper chalcopyrite solar cells with varying gallium content (*GGI*) from 0.0 to 1.0 will be given. The chapter is divided into two parts. In the first, the defect spectra of samples with different gallium content are described and compared in view of any *GGI* dependent changes. The second one deals with the defect signals occurring in the temperature range below 200 K. Some interesting properties are described and a peak width analysis is presented.

5.1 Experimental conditions

Typically the measurements were performed in a temperature range from 30 K or 60 K to 350 K. For the AS investigations, an a.c. voltage with an amplitude of 0.03 V was applied. Concerning the DLTS measurements, the reverse bias U_R was -1.5 V, the amplitude of the voltage pulse U_1 superimposed to the reverse bias was 1.5 V, and the width of the voltage pulse t_p was 1 s, if not explicitly mentioned. To ensure defined starting conditions, the samples investigated were almost always annealed 1 h at 350 K in the dark prior to measurement.

5.2 Defect spectra of the $\text{CuIn}_{1-x}\text{Ga}_x\text{Se}_2$ alloy system

The description of the defects occurring is split into two sections. First one deals with samples with mixed absorber composition, as these samples show similar defect spectra. Afterwards the deep levels occurring in CuInSe_2 and CuGaSe_2 are presented.

5.2.1 Devices with mixed absorber composition

In majority carrier DLTS performed with a voltage pulse height of $U_1 = 1.5$ V, only three negative majority carriers signals, i.e., hole traps in these devices, are observed (see figures 5.1(a) and (b), figure 5.2 and figure 5.3(a)).

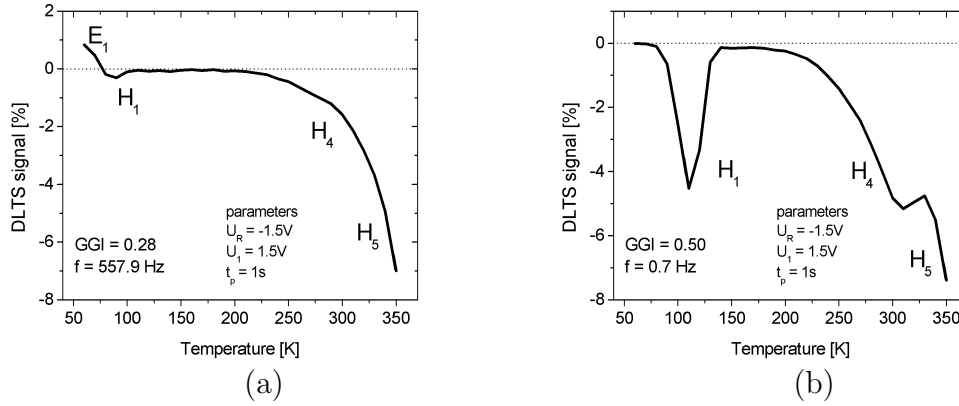


Figure 5.1: (a) DLTS signal versus temperature diagram of a Cu(In,Ga)Se₂ based solar cell with $GGI = 0.28$. The parameters are $U_R = -1.5$ V, $U_1 = 1.5$ V and $t_p = 1$ s. The boxcar frequency was 557.9 Hz. (b) DLTS signal versus temperature diagram of a Cu(In,Ga)Se₂ based solar cell with $GGI = 0.50$. The parameters are $U_R = -1.5$ V, $U_1 = 1.5$ V and $t_p = 1$ s. The boxcar frequency was 0.7 Hz.

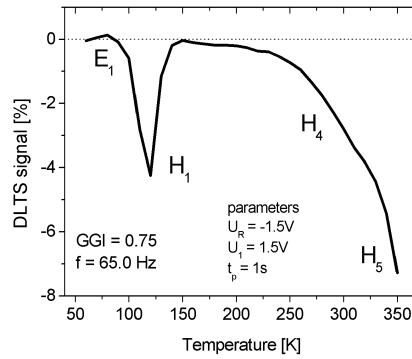


Figure 5.2: DLTS versus temperature diagram for a Cu(In,Ga)Se₂ based solar cells with $GGI = 0.75$ shown for a boxcar frequency equal to 65.0 Hz. The measurement parameters are the following: $U_R = -1.5$ V, $U_1 = 1.5$ V, $t_p = 1$ s.

The one in the temperature range below 200 K will be named "H₁", the other occurring at about 300 K, will be referred to as "H₄". The third signal

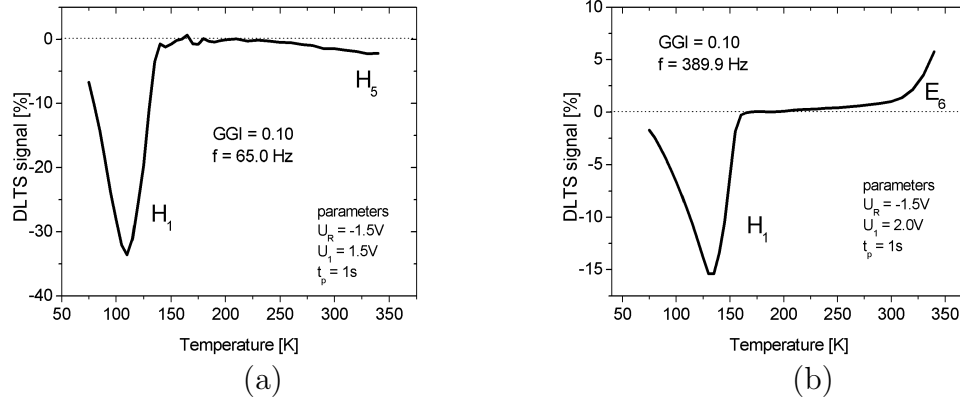


Figure 5.3: (a) Majority carrier DLTS signal versus temperature diagram of a $\text{Cu}(\text{In},\text{Ga})\text{Se}_2$ based solar cell with $GGI = 0.10$. The parameters are $U_R = -1.5$ V, $U_1 = 1.5$ V and $t_p = 1$ s. The boxcar frequency was 65.0 Hz. (b) Minority carrier DLTS signal versus temperature diagram of a $\text{Cu}(\text{In},\text{Ga})\text{Se}_2$ based solar cell with $GGI = 0.10$. The parameters are $U_R = -1.5$ V, $U_1 = 2.0$ V and $t_p = 1$ s. The boxcar frequency was 389.9 Hz.

called " H_5 " is only partly visible in the temperature range up to 350 K that is accessible with the experimental setup used. Under injection conditions, i.e., in minority carrier DLTS when a voltage pulse of $U_1 = 2.0$ V is superimposed to U_R , a positive electron trap signal " E_6 " develops for all mixed absorber compositions instead of H_5 in about the same temperature range (see figure 5.3(b)). Mostly the hole trap signal H_4 is not visible in these spectra either, but because the positive signal E_6 is very broad, it cannot be clearly determined, whether an additional electron trap signal is responsible for it or whether it is E_6 alone. Few and far between, the electron defect signal E_6 can also be detected in majority carrier DLTS for samples with GGI equal to 0.1, although in this mode one should only be able to detect majority defects. However, such phenomenon was observed earlier in Schottky diodes, too, and assigned to filling of minority carrier traps by leakage currents [95].

In admittance measurements, only one defect signal is found for the devices with $0 < GGI < 1$ as shown in figure 5.4(a). (The low temperature signal at about 100 K stems from the free charge carrier freeze out.) Comparing the AS and DLTS data in one common Arrhenius diagram points out that the defect detected with admittance spectroscopy corresponds to the low temperature hole trap H_1 as shown in figure 5.4(b). Yet, the Arrhenius plots are not strictly linear. Especially at lower temperatures, the data exhibit a pronounced curvature which has been attributed to a non-negligible influence of tunneling in this temperature range [92]. The latter is also re-

flected by sometimes obviously differing activation energies determined from AS and DLTS measurements for a respective value of GGI . Therefore the data are only considered as apparent or effective defect parameters. As the activation energy of H_1 varies in a considerable range for different samples of a special GGI , but also when comparing the samples of different GGI , a Meyer-Neldel evaluation was performed to determine, whether the trap signals detected stem from the same defect. (All activation energies given within this chapter were calculated neglecting the temperature dependence of the pre-exponential factor [102].) The respective diagram shown in figure 5.5 gives strong indication of a common origin for the signals investigated. Only the defect parameters obtained from a fit to the Arrhenius data of admittance measurements at the six highest temperatures were used for this diagram to reduce the impact of tunneling contributions. For the same reason, the respective DLTS data were not taken for the graph. From a linear fit the Meyer-Neldel parameters E_0 and ν_{00} were obtained. The values are 31 meV and $6.6 \times 10^7 \text{ s}^{-1}$. These numbers are in good agreement with those from similar investigations on damp-heat treated and as-grown $\text{Cu}(\text{In},\text{Ga})(\text{S},\text{Se})_2$ based solar cells, respectively. There, E_0 was about 29 meV (32 meV) and ν_{00} about $1.3 \times 10^7 \text{ s}^{-1}$ ($8 \times 10^7 \text{ s}^{-1}$) [103, 104].

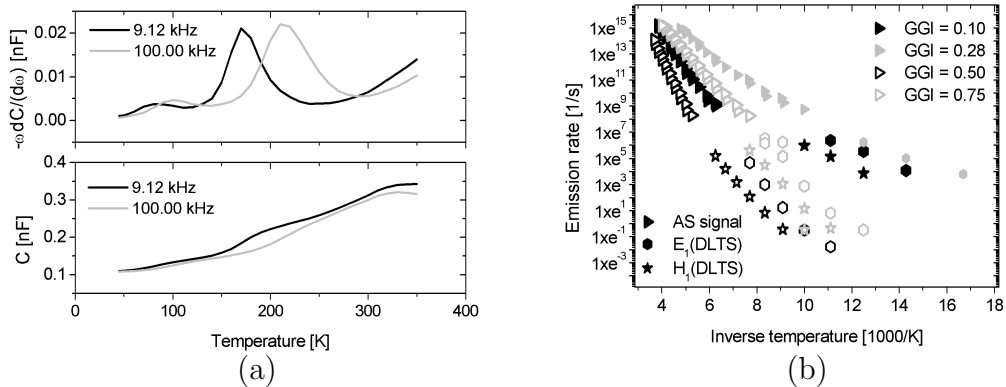


Figure 5.4: (a) Capacitance (bottom) resp. $-\omega dC/d\omega$ (top) versus temperature diagram of a $\text{Cu}(\text{In},\text{Ga})\text{Se}_2$ based solar cell with $GGI = 0.50$ at 9.12 kHz (dark curves) and 100.00 kHz (gray curves) modulation frequency. (b) Comparison of AS and DLTS signals of $\text{Cu}(\text{In},\text{Ga})\text{Se}_2$ based solar cells with different gallium content in one common Arrhenius diagram. Shown are data for the AS signal (triangles) and the DLTS signals E_1 (hexagons) and H_1 (stars). The respective samples have a GGI of 0.10 (full black symbols), 0.28 (full gray symbols), 0.50 (open black symbols), and 0.75 (open gray symbols).

Another aspect that has to be noted concerning H_1 is the remarkable behavior of the defect signal when changing measurement parameters as length

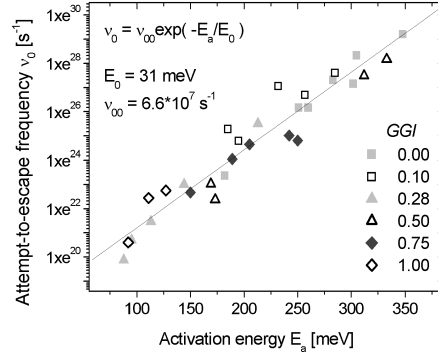


Figure 5.5: Meyer-Neldel diagram and linear fit of the defect parameters determined from admittance spectroscopy for the six highest temperatures.

or height of the voltage pulse applied. The exceptional properties are, in principle, observed for devices of all GGI values examined. A detailed description will be given in section 5.3. However, for completeness of the defect spectra description, the experimental findings shall be briefly summarized in this section, too. Depending on the measurement conditions, one detects either the negative hole trap signal H_1 or a positive electron trap signal at slightly lower temperatures (which is called " E_1 ") or a combination of both. The trap signals E_1 and H_1 mostly show quite similar deep-level parameters. Taking further into account that in admittance only one trap signal could be observed, it is possible that these two signals of opposite sign belong to the same defect. However, the reason for the complex defect behavior observed in various measurements remains unknown so far.

5.2.2 CuInSe_2 and CuGaSe_2 based devices

The AS spectra of the devices with CuInSe_2 and CuGaSe_2 absorbers show two defect signals (see figures 5.6(a) and (b)). For CIS, the defects have activation energies ranging from about 170 meV to 350 meV and about 510 meV to 710 meV (named " a " and " b ", respectively). The defects detected for CGS exhibit activation energies extending from about 90 meV to 130 meV and 290 meV to 310 meV (called " c " and " d ", respectively).

Concerning the DLTS measurements performed on CIS based devices, the defect signals E_1/H_1 , H_4 and H_5 , already known from the mixed absorber compositions, are also present. The low temperature signals E_1/H_1 again correspond to the defect b seen in AS. Additionally, the samples exhibit one more trap signal in DLTS: an electron trap, called " E_3 ", at about 250 K (figure 5.7(a)). As the latter minority carrier signal is in close vicinity to

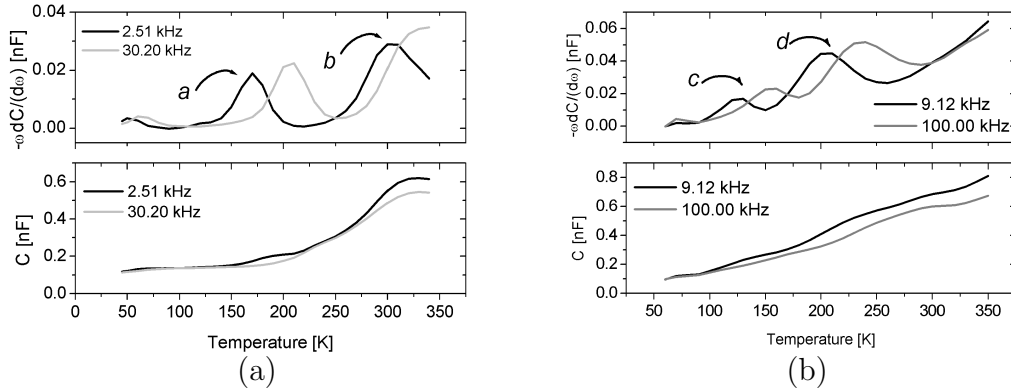


Figure 5.6: (a) Capacitance (bottom) resp. $-\omega dC/d\omega$ (top) versus temperature diagram of a CuInSe₂ based solar cell at 2.51 kHz (dark curves) and 30.20 kHz (gray curves) modulation frequency. (b) Capacitance (bottom) resp. $-\omega dC/d\omega$ (top) versus temperature diagram of a CuGaSe₂ based solar cell at 9.12 kHz (dark curves) and 100.00 kHz (gray curves) modulation frequency.

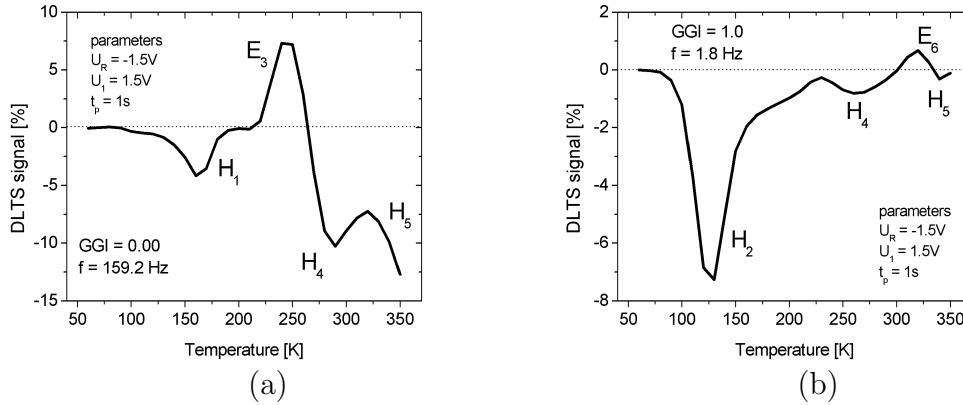


Figure 5.7: (a) DLTS signal versus temperature diagram of a CuInSe₂ based solar cell. The parameters are $U_R = -1.5$ V, $U_1 = 1.5$ V and $t_p = 1$ s. The boxcar frequency was 159.2 Hz. (b) DLTS signal versus temperature diagram of a CuGaSe₂ based solar cell. The parameters are $U_R = -1.5$ V, $U_1 = 1.5$ V and $t_p = 1$ s. The boxcar frequency was 1.8 Hz.

the hole trap (H_4), one observes a scatter in activation energies for these two signals. Especially, those for the signal E_3 are actually too large to be realistic. Drawing the data of these DLTS signals together with the defect state b detected by AS in one common Arrhenius diagram, it seems to be likely that b either corresponds to E_3 or H_4 (see figure 5.8). Unfortunately, a more precise assignment is not possible. The high temperature defect

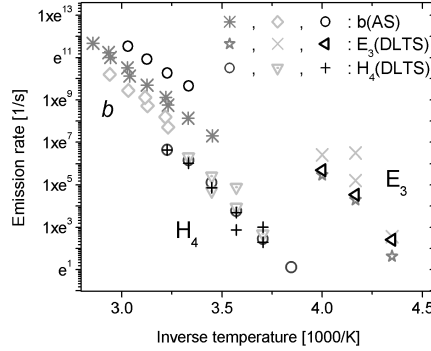


Figure 5.8: Comparison of AS and DLTS signals of CuInSe_2 based solar cells in one common Arrhenius diagram. For each defect signal b , E_3 and H_4 , the results from three different measurements are shown to demonstrate the problem of assigning the admittance signal b either to E_3 or H_4 .

signal E_6 cannot be clearly seen in CIS. However, this might be due to the large amplitude of the defect signal H_5 even in minority carrier DLTS so that E_6 might be visible only at temperatures higher than 350 K. One comment has to be made on H_4 and H_5 : although in CIS the respective signals occur at slightly lower temperatures compared to the mixed absorber compositions, these defect signals are very likely to coincide with those found for the other GGI values as the temperature shift compared to the mixed absorber compositions can be attributed to the influence of the additional defect signal E_3 and/or the different amplitude ratio of the defects.

In the CGS samples, the defect signals H_4 , H_5 , and E_6 are observed as shown in figure 5.7(b). The high temperature electron trap (E_6) is here also seen under non-injection conditions, i.e., in majority carrier DLTS. Again, a small shift of H_4 and H_5 to lower temperatures as observed in the CIS samples is found. The electron trap signal E_1 is visible, too, but again only in measurements with small voltage pulse height (0.3 V). Yet, the trap signal H_1 cannot be detected in the CGS samples because it is covered by an additional hole trap " H_2 ". Comparison of AS and DLTS data demonstrate that the trap signal E_1 corresponds to the defect signal c found in AS whereas the DLTS signal H_2 coincides with signal d detected by AS. This issue will be presented in detail in section 5.3.3 and is here just mentioned for a complete description of the defect spectra in general.

The sign of all defect signals occurring in DLTS was verified by evaluation of transient conductance data in order to exclude any signal inversion. In contrast to capacitance transients which can give a false sign due to a non-negligible series resistance, the respective conductance values are not affected

in this way and therefore give the correct sign [94]. Table 5.1 summarizes the proceeding description and gives the ranges of activation energies determined for the respective defects.

Table 5.1: Summary of the defect signals from AS and DLTS measurements detected for different absorber compositions. If possible the range of activation energy determined is given. The symbols "x" and "-" indicate, that a distinct defect does occur and does not occur, respectively.

DLTS					
GGI	E_1/H_1	H_2	E_3	H_4	H_5/E_6
0.00	x/x	-	x	x	x/-
0.10	x/x	-	-	(x)	(x/x)
0.28	x/x	-	-	(x)	x/x
0.50	x/x	-	-	(x)	(x/x)
0.75	x/x	-	-	(x)	(x/x)
1.00	x/-	x	-	x	x/x
E_a (DLTS) [meV]	30 - 280/ 50 -280	220 - 310	860 - 1280	470 - 850	700-1340/ 880-1290
AS					
E_a (AS) [meV]	90-350	290-310	510-710 ⁺		-

(): E_a could not be determined for this GGI

+: AS signal only for $GGI = 0.00$

5.3 The defect signals below 200 K

As already indicated briefly in the preceding section, the two defect signals E_1 and H_1 which occur in the temperature range $T < 200$ K exhibit some remarkable properties. At first, these are described for copper chalcopyrite solar cells with GGI smaller than 1.0, as there, the exceptional behavior is clearly seen. Secondly, the CuGaSe₂ samples are considered, where an additional signal somewhat covers the properties of interest. Lastly, a peak width analysis on E_1 and H_1 is presented.

5.3.1 CuInSe₂ and Cu(In,Ga)Se₂ absorbers with different gallium content

The exceptional behavior of the defect signals E_1 and H_1 are revealed in several experiments by variation of a certain measurement parameter like

reverse bias level U_R , height of the superimposed voltage pulse U_1 or length of the voltage pulse t_p . Additionally, detailed examination of the change in capacitance during the whole measurement procedure was performed, in "conventional" DLTS and RDLTS mode.

Variation of the reverse bias voltage U_R

The variation of the reverse bias level U_R , while keeping the voltage pulse height U_1 fixed, is actually a method to determine concentration profiles of trap levels using DLTS [74]. The space charge region is scanned using different levels of reverse bias and a constant, relatively small height of voltage pulses. Furtheron, this kind of experiment will be called " U_R variation". The results from these measurements can be described as follows: irrespective of the level of reverse bias voltage which was varied from -0.3 V to -1.5 V, always a minority carrier signal was detected as shown in figure 5.9(a). This positive signal is named E_1 . The amplitude of the trap signal somewhat decreases with increasing reverse bias. The bias dependence is probably due to a non-negligible width of the transition region λ between the space charge region and the bulk which can lead to the aforementioned behavior [77]. It should be noted that a relatively small voltage pulse U_1 of 0.3 V was applied, as this will be important for a comparison of the U_R variation to the measurement described in the next section.

Variation of the voltage pulse height U_1

In another experiment, the height of the voltage pulse is varied, and the reverse bias level is kept fixed (called " U_1 variation" in the following). This is an alternative technique to investigate concentration depth profiles of deep levels [74]. The observation volume within the space charge region is increased from the depletion region edge towards the p-n junction interface with increasing height of voltage pulse. A plot of the signal amplitude versus height of the voltage pulse therefore provides insight into a deep level concentration profile. A linear behavior, for instance, indicates a profile proportional to the doping profile of the sample. Generally, the DLTS versus temperature spectra obtained at different heights of the voltage pulse show the following behavior (see figure 5.9(b)): If the voltage pulse applied is relatively small, the positive signal E_1 is detected. With increasing pulse height, the minority carrier signal decreases, and a majority carrier signal (named H_1 as mentioned in section 5.2) starts to grow in. This "pulse height dependent sign change" occurs within a relatively small range of voltage pulse heights, mostly a few tenth of millivolts. It should be noted, that the phenomena described, in principle, are observed for samples of all GGI values investigated. However, for the solar cells with GGI equal to 0.28, the pulse

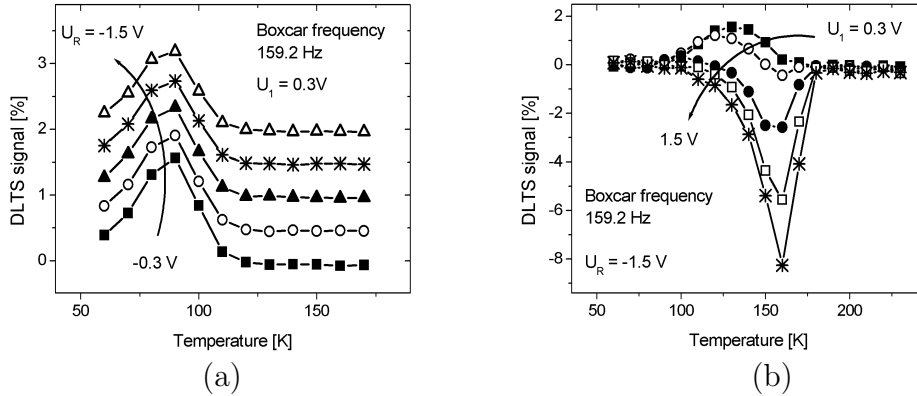


Figure 5.9: (a) DLTS signal versus temperature diagram of a Cu(In,Ga)Se₂ based solar cell with $GGI = 0.10$ under variation of the reverse bias from - 0.3 V to - 1.5 V ($\Delta U_R = 0.3$ V). The parameters $U_1 = 0.3$ V and $t_p = 1$ s were kept constant. The boxcar frequency was 159.2 Hz. The spectra were shifted for clarity. (b) DLTS signal versus temperature diagram of a Cu(In,Ga)Se₂ based solar cell with $GGI = 0.50$ under variation of the voltage pulse height U_1 from 0.3 V to 1.5 V ($\Delta U_1 = 0.3$ V). The parameters $U_R = -1.5$ V and $t_p = 1$ s were kept constant. The boxcar frequency was 159.2 Hz.

height dependent sign change is often not completed for U_1 equal to 1.5 V. That means, besides signal H_1 , the defect signal E_1 is still observed at this voltage pulse height, whereas for devices of other GGI , E_1 has vanished, and H_1 is exclusively detected. The striking aspect of the defect parameters is that the values obtained for the minority and the majority carrier trap are quite similar. The apparent activation energies E_a for the minority carrier signal (determined at U_1 equal to 0.3 V) and the majority carrier signal (at U_1 equal to 1.5 V) are listed in table 5.2. The actual activation energies should again be taken only as approximate or apparent values, as sometimes the signals can be evaluated only in a narrow temperature range and the temperature dependence of the pre-exponential factor was neglected. In AS measurements performed on the respective samples, only one defect level was revealed as shown in figure 5.4(a).

Variation of the voltage pulse length t_p

As third variation measurement, the pulse length was varied at a certain height of voltage pulse. This method will be called “ t_p variation“ in the following. A measurement with U_1 equal to 0.48 V shows figure 5.10(a). For a short voltage pulse, the signal H_1 dominates the spectrum. With increasing pulse length, the negative signal decreases, and the positive signal E_1 comes into play. The general trend, i.e., a decrease in H_1 respectively an increase

Table 5.2: Activation energies of the defect signals E_1 , H_1 and H_2 determined by DLTS for different absorber compositions. In the CGS samples, signal H_1 is probably covered by the additional defect H_2 and, therefore, cannot be detected (see paragraph 5.3.3).

GGI	$E_a(E_1)$ [meV]	$E_a(H_1)$ [meV]	$E_a(H_2)$
0.00	220-280	220-280	–
0.10	60-80	70-100	–
0.28	30-50	50-60	–
0.50	150-190	150-180	–
0.75	120-160	130-170	–
1.00	100-140	–	290-310

in E_1 with increasing pulse length is observed for all heights of the voltage pulse, even if the sign change does not occur (not shown).

Observation of the voltage pulse

In addition to the experiments described so far, the changes in the sample capacitance not only after perturbation by the voltage pulse, but also during its application were monitored. The latter was done for the U_1 and the t_p variation measurements at a distinct temperature. In figure 5.10(b), the time development of the changes in device capacitance ΔC before ($t < 10^{-3}$ s), during (10^{-3} s $\leq t \leq 1$ s) and after ($t > 1$ s) application of the voltage pulse is shown. Before pulse application and long time afterwards, ΔC approaches the same level which indicates that the perturbation induced by the voltage pulse is reversible. (The deviation of ΔC from zero before perturbation and after return to equilibrium, respectively, stems from imperfect balancing the sample's equilibrium capacitance and the limited reading of this residual capacitance offset.) However, the most remarkable aspect is the development of ΔC during the voltage pulse application. Usually, at the beginning of the voltage pulse, one expects an abrupt rise in capacitance due to the reduced potential difference which is followed by an exponential decay in case of capture of majority carriers and an exponential saturation in case of capture of minority carriers, respectively. In contrast to that, the experimental data in figure 5.10(b) show, that ΔC abruptly falls to values smaller than zero and then increases steadily during the filling process.

In another experiment, the temporal development of the device capacitance in the reverse bias DLTS mode was compared with conventional majority carrier DLTS measurements. In reverse DLTS (abbreviated RDLTS),

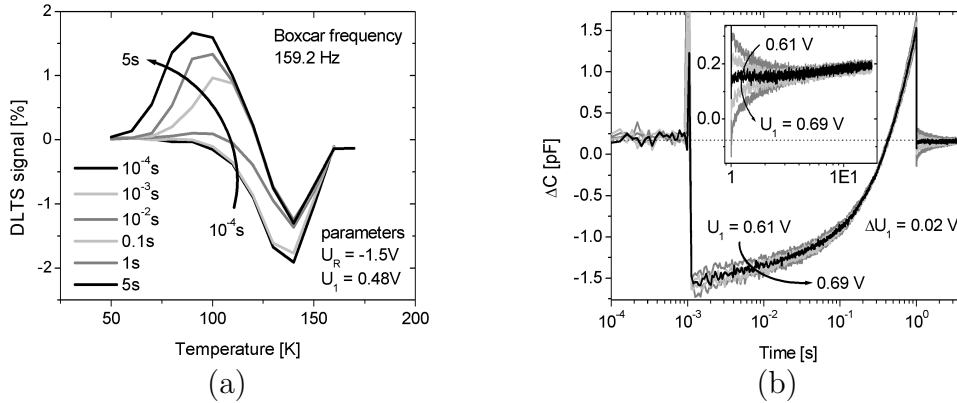


Figure 5.10: (a) DLTS signal versus temperature diagram of a Cu(In,Ga)Se₂ based solar cell with $GGI = 0.10$ under variation of the pulse length t_p from 10^{-4} s to 1 s. The parameters $U_R = -1.5$ V and $U_1 = 0.48$ V were kept constant. The boxcar frequency was 159.2 Hz. (b) Time dependent changes in capacitance of a Cu(In,Ga)Se₂ based solar cell at 120 K with $GGI = 0.50$ before (0 s to 10^{-3} s), during (10^{-3} s to ≈ 1 s) and after ($t > 1$ s) application of the voltage pulse. The voltage pulse height U_1 was varied from 0.61 V to 0.69 V ($\Delta U_1 = 0.02$ V); the parameters $U_R = -1.5$ V and $t_p = 1$ s were kept constant. Note the unusual decrease in capacitance ($\Delta C < 0$ pF) immediately after voltage pulse application. (The overshoot at the beginning of the voltage pulse is due to the dead time of the capacitance bridge.)

one increases the reverse bias level (we always refer to the absolute value of reverse bias) during application of the voltage pulse. Therefore, traps are emptied and, after its application, one actually observes recapture of charge carriers [78]. Such procedure exactly corresponds to the opposite of the conventional DLTS technique, where the thermally activated emission of charge carriers is monitored after filling these traps by reduction of the bias level. The only difference between those measurement techniques is that, because of the opposite direction of the voltage pulse applied, one observes the different processes at different times of the measurement sequence: increase in bias level takes place, for example, in RDLTS during the first part of the experiment, i.e., the actual application of the voltage pulse, whereas in conventional DLTS it is related to the second part of the experiment, i.e., the time interval after voltage pulse application.

The capacitive detection of the whole voltage pulse sequence in one RDLTS measurement reveals that the changes correspond to those observed in the conventional DLTS experiment: If the increase in reverse bias level is small (see figure 5.11(a): RDLTS: part 1 of the experiment; DLTS: part 2 of the experiment), one observes a reduction of the capacitance which corresponds

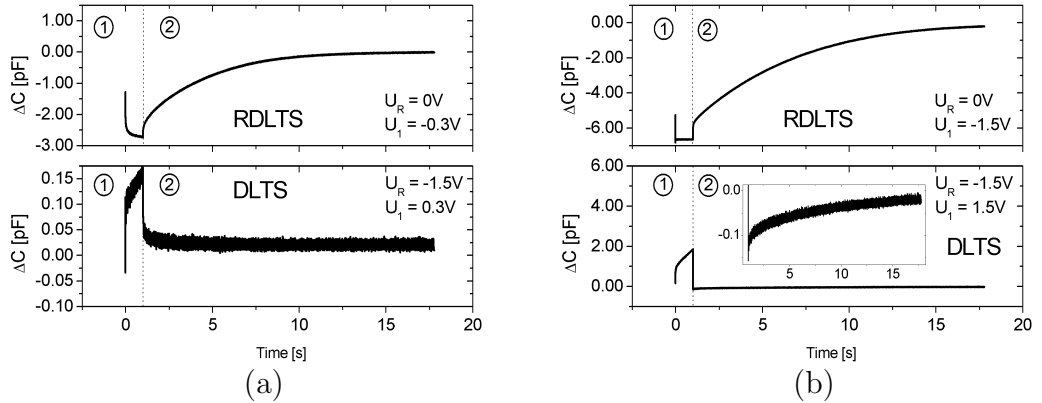


Figure 5.11: (a) Time development of the capacitance of a Cu(In,Ga)Se_2 based solar cell with $GGI = 0.75$ during and after application of a voltage pulse with small amplitude; upper diagram: RDLTS, lower one: DLTS. The parameters $U_R = -1.5$ V, $U_1 = 0.3$ V, and $t_p = 1$ s (DLTS) resp. $U_R = 0$ V, $U_1 = -0.3$ V, and $t_p = 1$ s (RDLTS) were kept constant. The temperature was 120 K. (b) Time development of the capacitance of a Cu(In,Ga)Se_2 based solar cell with $GGI = 0.75$ during and after application of a voltage pulse with large amplitude; upper diagram: RDLTS, lower one: DLTS. The parameters $U_R = -1.5$ V, $U_1 = 1.5$ V, and $t_p = 1$ s (DLTS) resp. $U_R = 0$ V, $U_1 = -1.5$ V, and $t_p = 1$ s (RDLTS) were kept constant. The temperature was 120 K.

to emission of minority carriers. If the increase in reverse bias is relatively large (see figure 5.11(b): RDLTS: part 1 of the experiment; DLTS: part 2 of the experiment), an increase in capacitance is monitored which corresponds to emission of majority carriers. After reduction of the reverse bias level, one always detects a capture of minority carriers, i.e., an increase in capacitance, irrespective of the pulse height (see figures 5.11(a) and (b): RDLTS: part 2 of the experiment; DLTS: part 1 of the experiment).

5.3.2 Check of signal direction

As the leakage current of the copper chalcopyrite solar cells investigated does not saturate but increases steadily with increasing reverse bias level, the direction of the measured capacitance transients was checked to exclude any sign inversion to be responsible for unexpected results described before, for example the different results from U_R and U_1 variation and the unusual behavior in the t_p variation experiment.

In contrast to section 5.2, where the conductance transients were consulted, this time an additional resistance R_s connected in series to the device under test was used (see section 4.3.6). The result is shown in figure 5.12(a)

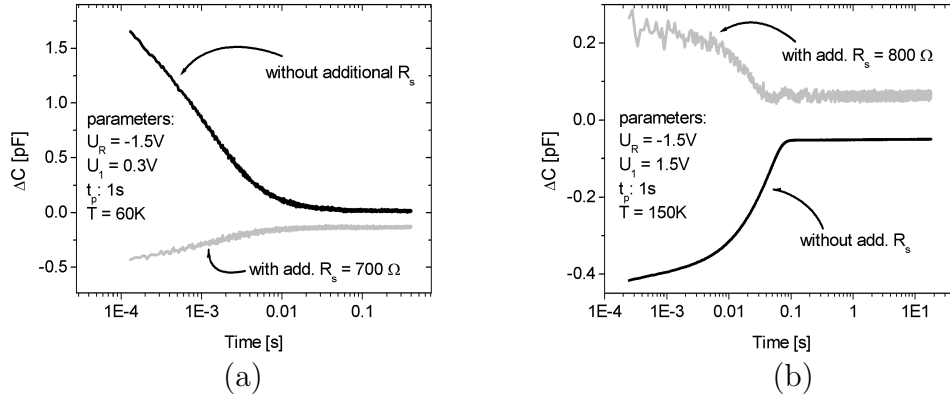


Figure 5.12: (a) Capacitance transient of a solar cell with $GGI = 0.28$ after application of a 0.3 V high voltage pulse without (black curve) and with an additional series resistance of 700 Ω . The temperature was 60 K, the reverse bias voltage U_R was -1.5 V and the length of the voltage pulse t_p was 1 s. (b) Capacitance transient of a solar cell with $GGI = 0.50$ after application of a 1.5 V high voltage pulse without (black curve) and with an additional series resistance of 700 Ω . The temperature was 150 K, the reverse bias voltage U_R was -1.5 V and the length of the voltage pulse t_p was 1 s.

for the signal E_1 testing a solar cells with GGI equal to 0.28 and in figure 5.12(b) for the signal H_1 from a solar cell with $GGI = 0.50$. The positive and the negative capacitance transient, respectively, could be inverted by addition of a series resistance. This means, that the original sign of these transients is correct and a non-negligible series resistance as explanation for the exceptional properties found can be excluded.

5.3.3 CuGaSe₂ absorbers

Solar cells with CuGaSe₂ absorber, in principle, exhibit properties similar to those stated for the samples with absorber layer of lower gallium content, but there the situation appears to be more complicated. The DLTS spectra obtained under variation of U_R or U_1 are comparable to the respective ones for the Cu(In,Ga)Se₂ and CuInSe₂ samples. The only difference is that, even for small voltage pulse levels, both a minority carrier and a majority carrier signal are detected. The apparent activation energy for the positive signal is about 100 meV to 140 meV. However, as the signal has a fairly small amplitude and can be evaluated just in a narrow temperature range, these values for E_a should be only taken as approximate ones. For the majority trap level, E_a is about 220 meV to 310 meV. As indicated in section 5.2.2, the trap signal shall be named " H_2 ", as later it will become clear that the

signal is different from H_1 .

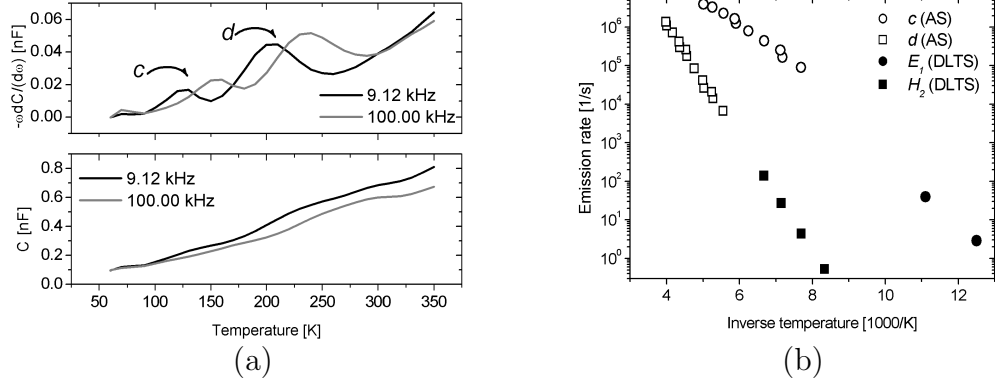


Figure 5.13: (a) Capacitance (bottom) resp. $-\omega dC/d\omega$ (top) versus temperature diagram gained from AS on a CuGaSe₂ based solar cell at 9.12 kHz (dark curves) and 100.00 kHz (gray curves) modulation frequency. (b) Comparison of AS and DLTS signals of a CuGaSe₂ based solar cell in one common Arrhenius diagram. The data indicate that the high temperature AS signal d (open squares) and the additional majority carrier DLTS signal H_2 (full squares) belong to the same defect. The same seems to hold for the AS signal c (open circles) and the DLTS signal E_1 (full circles). However, the defect signal H_1 cannot be evaluated in CuGaSe₂ based solar cells due to an overlap with signal H_2 .

A closer look at the shape of the negative peak gives rise to the assumption that it actually consists of at least two different negative signal components or exhibits a tail-like distribution of trap states towards higher energy. The corresponding AS measurements confirm this notion, concerning H_1 and H_2 . The AS spectrum (see figure 5.13(a)) exhibits two trap levels that are quite close to each other. For the one developing at lower temperatures (called "c" in figure 5.13(a)), an activation energy E_a ranging from about 110 meV to 120 meV was determined. The activation energy of the other one (called "d") ranges from about 290 meV to 310 meV. Plotting the trap level parameters from AS and DLTS measurements in one common Arrhenius diagram, it is very likely that both the trap level d and the negative DLTS signal H_2 do belong to the same defect (see figure 5.13(b)). The same holds for trap level c and signal E_1 detected via AS and DLTS, respectively. If one considers now that for the devices with mixed absorber composition, only one defect signal was detected which coincides with the DLTS defect signals E_1 and H_1 , it becomes clear that H_2/d has to be an additional defect occurring exclusively in the CGS samples investigated. The above comparison leads to the conclusion that the minority carrier signal E_1 and the defect c correspond to the trap level with the interesting features mentioned above, whereas signal

H_2 and the defect level d represent an additional majority carrier defect that partially covers the aforementioned properties of the other defect signal, for instance, the pulse height dependent sign change.

5.3.4 Peak width analysis

For the defect signals E_1 and H_1 , a peak width analysis was performed. These are the only ones that are clearly visible and appropriately separated for all GGI . However, in the case of CGS, the procedure could not be carried out for H_1 , as the signal is not detected in these samples. There are also only few data available for the analysis of E_1 as the signal is sometimes too small to be analyzed in CGS.

Theoretically, the evaluation of exponential DLTS transients applying the boxcar weighting function leads to DLTS signals with a relative peak width of

$$\Delta T/T_{max} = \ln(16.5)/(2 + E_a/(kT)) \quad (5.1)$$

which is usually ≈ 0.1 , as described in section 4.3.4.

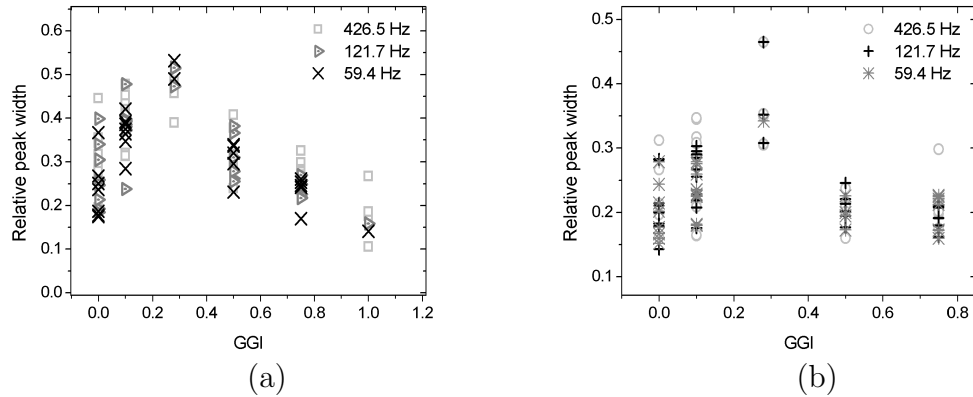


Figure 5.14: (a) Peak width versus GGI diagram for the defect signal E_1 . The data are shown for three different boxcar frequencies: 426.5 Hz (squares), 121.7 Hz (triangles), 59.4 Hz (crosses). (b) Peak width versus GGI diagram for the defect signal H_1 . The data are shown for three different boxcar frequencies: 426.5 Hz (circles), 121.7 Hz (crosses), 59.4 Hz (triangles).

If the transient for some reason is non-exponential, the DLTS peaks width is larger than the theoretical value calculated from the equation above. So, the relative peak width provides a measure to evaluate the degree of “non-exponentiality“ of a defect emission signal. The results are shown in figures 5.14(a) and (b) as relative peak width versus GGI diagrams for three different boxcar frequencies. Both graphs indicate some change in relative peak width with gallium content: the maximum peak width is observed at GGI equal

to 0.28 for both trap signals, E_1 and H_1 . However, if one looks at the ratio of experimental and theoretical peak width calculated from the temperature at the peak extrema and the determined activation energies, a somewhat different result is obtained. As shown in figure 5.15(a), no clear dependence of the normalized relative peak width on the gallium content can be determined, for all GGI peak broadening, i.e. a normalized peak width larger than one, is found. Yet, a pronounced scatter in values, especially for the signal E_1 at GGI equal to 0.0, has to be stated, so that the extend of peak broadening is hard to analyze.

In contrast to that, a slight dependence on the gallium to gallium plus indium ratio is visible for the apparent activation energies of E_1 and H_1 determined from the same DLTS measurements. A decrease in activation energy is observed up to a GGI of 0.28 with increasing gallium content. For a GGI of 0.50, E_a rises a little again and then level off at a certain value for gallium contents larger than 0.50. However, a slight reduction in activation energy for GGI larger than 0.50 is visible. However, this might be caused by the scatter in values determined.

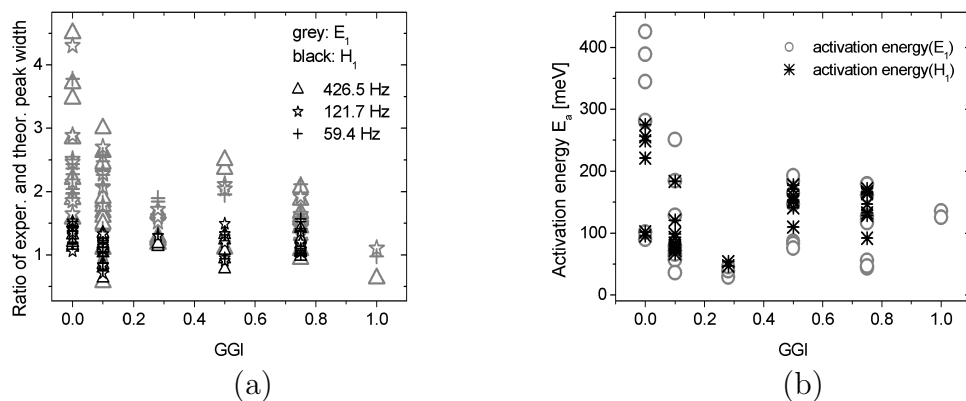


Figure 5.15: (a) Relative peak width normalized to the respective theoretical value (calculated using equation 4.20) versus GGI diagram for the defect signals E_1 (grey symbols) and H_1 (black symbols). The data are shown for three different boxcar frequencies: 426.5 Hz (triangles), 121.7 Hz (stars), 59.4 Hz (crosses). (b) Activation energies versus GGI diagram for the defect signals E_1 (grey circles) and H_1 (black crosses).

Chapter 6

Discussion

Within this chapter, the experimental results presented before are discussed. For clarity the different issues are addressed again in separate sections. Firstly, the defect spectra in general are dealt with. Here, the discussion also includes earlier results reported in literature and compares them to the experimental findings obtained within this thesis. The second part provides a detailed discussion about the origin of exactly these trap signals. The last section is about peak broadening found for the defect signals E_1 and H_1 .

6.1 The defect spectra of the In-Ga alloy system

In the following the experimental findings presented shall be compared to earlier measurements reported. First of all, the defect signals E_1 and H_1 are looked at.

In literature, mostly the minority carrier trap signal E_1 was observed exclusively. It is often referred to as N_1 or β [65, 105, 106]. Thermal activation energies in the range of 0.1 to 0.3 eV were reported. In addition to the unusual observation of a minority carrier trap signal in majority carrier DLTS, i.e. without injection of minority carriers, DLTS and AS investigations showed that the apparent activation energy of this trap level changes depending on the treatment applied to the device under test prior to the measurement. Such a pretreatment can be annealing or illumination of the sample or application of a bias voltage to it. These experimental findings led to the interpretation of this defect signal as a band of interface defects where the Fermi level is pinned at the interface, i.e. the shift in Fermi level position is only small even if the change in bias level is comparably large. Within this frame, the pretreatments were believed to cause a respective shift in Fermi level position and therewith induce the observed changes in activation energy [8, 106, 107]. However, there are also some experimental

findings that contradict the above mentioned interpretation. If one deals with an interface defect in an AS measurement, the high frequency value of capacitance corresponds to the total width of the depletion region whereas the height of this capacitance step gives the width of the depletion layer in the n-type region of the device (for the CIGS solar cell structure) [107]. Yet, for the CIGS solar cells, the respective experimental data give an unrealistic large extension of the space charge region into the n-type region [67, 108]. Moreover, an influence of this defect signal (N_1, β) on the doping profile was found. These two aspects are more consistent with a bulk than an interface defect [67]. To solve this problem, dealing on the one hand presumably with a bulk defect but observing pretreatment dependent changes in activation energies on the other hand, Igalson and Edoff [109] proposed that there exist two charge states of the above mentioned low temperature defect level, where the second state in most samples is only visible after electron injection by application of a forward bias or illumination.

Coming now to H_1 , it can be said that the negative majority signal is only rarely reported [110]. Within the article from Deibel et al. [110], the defect signal is called " γ " and interpreted as trap level independent of E_1 . The coupling between E_1 and H_1 observed within this thesis has not yet been observed.

After summarizing the aspects known about these defect signals in literature so far, they shall be critically analyzed. Because of the exceptional behavior of E_1 and H_1 described in sections 5.2 and 5.3, their interpretation as two independent defects can be excluded. In fact, the situation seems to be way more complex than the issue whether one deals with an interface or a bulk related defect, as a mechanism has to be found than can account for the sign inversion observed. Neglecting that the ansatz from Igalson and Edoff does not deal with H_1 either, their interpretation of the positive trap signal as defect level with two different charge states could explain the large range of activation energies obtained for samples with one distinct GGI (see section 5.2). On the other hand, this model is contradictory to the fact that the defect parameters extracted from AS measurements presented within this thesis fulfill the Meyer-Neldel relation, as demonstrated in figure 5.5. So, this aspect still remains an open question, too. However, the key prerequisite is surely to solve the issue of the sign change. Only then, the origin of the defect signals can be clarified. A detailed discussion of possible mechanisms will be given in section 6.2.

Secondly, we concentrate on H_2 . In earlier AS and DLTS measurements, a majority carrier defect named N_2 was found in CIS, CIGS, and CGS based solar cells. The corresponding deep level exhibited activation energies similar to those found for the trap signal H_2 . Hence, it is likely that trap H_2 coincides with defect N_2 [65, 106, 111]. Some tail-like extension to midgap reported for N_2 could at least qualitatively be detected in our measurements, too

[65]. However, it has to be noted that H_2 (or N_2) is exclusively visible in the CGS samples investigated within this thesis whereas N_2 was observed in CIS, CIGS and CGS samples. Yet, this might be due to an improved quality of the absorber material as the concentration of N_2 was found to be correlated with the solar cell efficiency [66].

Concerning the defect signals E_3 and H_4 , no comment on these signals could be found in literature. Therefore they seem to be detected for the first time.

Now, the trap signals H_5 and E_6 are addressed. In earlier DLTS measurements on CIGS based solar cells with GGI equal to 0.3, an electron and a hole trap signal were observed in about the same temperature range, too [110, 112]. The defect energies determined for the positive and the negative signal were both about 550 meV, so it was assumed that they stem from the same defect level, i.e., from a recombination center [110]. Photocapacitance measurements performed for Cu-chalcopyrite based solar cells covering the whole In-Ga alloy range revealed a high temperature defect signal with activation energy of about 800 meV [113]. As the latter moves closer to midgap with increasing band gap of the absorber layer ($E_G(\text{CIS}) = 0.98$ eV whereas $E_G(\text{CGS}) = 1.66$ eV [3]), the authors proposed that it might become an efficient recombination center in samples with higher gallium content. Taking the experience that the determination of activation energies – at least in DLTS for the high temperature signals – can be somewhat difficult into account, it is possible that the mentioned experimental findings, although they give quite different numbers for the activation energies, describe the same defect level. Despite the fact, that the activation energies determined within this thesis cover a broad range of values, the other properties of these signals, e.g., their occurrence in about the same temperature range and the replacement of H_5 by E_6 observed for the mixed absorber compositions, indicate that these high temperature defect signals coincide with those already described in literature.

Generally, the deep levels present in the indium-gallium alloy range can be described as follows: For the mixed absorber compositions, in principle, the same defects are present. These are the low temperature signals E_1/H_1 , the properties of which are not yet understood, and the three high temperature trap signals H_4 , H_5 , and E_6 . The defect signals H_5 and E_6 do very likely represent a recombination center. The "edge compositions" CIS ($GGI = 0$) and CGS ($GGI = 1$) exhibit somewhat different defect spectra. Concerning any systematic gallium dependent changes in defect spectra, the investigations did not reveal any new detrimental defect which might cause the (momentarily still) lower efficiencies of CIGS based solar cells with higher gallium content. In view of the "open circuit voltage problem" of devices with $GGI > 0.3$ the investigations lead to the conclusion that the bulk of the absorber material is not decisive concerning the sublinear increase in V_{OC} .

6.2 The trap signals E_1 and H_1

Considering the contradictory results from the two different defect concentration profiling techniques (U_R and U_1 variation), it can be stated that the results of these measurements cannot be interpreted as concentration gradients. As there are different puzzling aspects concerning the investigations presented in section 5.3, they shall be addressed separately.

Starting point is the fact that the trap parameters for the E_1 and the H_1 signal are quite similar. Either this is just a peculiar incident, because they influence each other considerably, or these two signals stem from the same defect level. Nevertheless, in both cases the explanation, why the sign of the signal changes depending on the measurement parameters, is not straightforward. One could argue that the “sign change” of the signals observed is only an artifact induced by the measurement procedure [93]. However, as mentioned in section 5.3.2, a misfit of the applied equivalent circuit (a capacitor in parallel to a resistor) due to a non-negligible series resistance can be excluded. Several plausibility checks with an additional resistor connected in series to our device under test demonstrate that the observed pulse height dependent sign change is definitely not induced by such an effect [114], as shown in figures 5.12(a) and (b).

Now, the actual emission signal is discussed: If one calculates the changes in electric field \mathbf{E} during the U_R and U_1 variation measurements, it becomes clear that \mathbf{E} changes much stronger in case of varying the height of the voltage pulse than it does for the measurements at different levels of reverse bias. However, the t_p variation where the influence of electric field should increase with increasing voltage pulses due to capture deeper in the depletion region shows the opposite sign change compared to the U_1 variation (see figures 5.9(b), 5.10(a)). Considering these findings, the electric field either is not the only decisive parameter or it does not play an important role in the explanation of the observations made on E_1 and H_1 .

From monitoring the course of the filling pulse during U_1 variation as shown in figure 5.10(b), it can be seen that the emission signal developing after voltage pulse application has to be a superposition of two contributions. This becomes obvious if one looks at the capacitance transient for U_1 equal to 0.65 V (pronounced dark curve in figure 5.10(b)). Here, the increasing capacitance during pulse application clearly indicates a transient change induced by the voltage pulse. In contrast to that, the subsequent relaxation to equilibrium shows almost no fast transient behavior. (The relatively slow negative contribution to the transient at time scales larger than 1 s is due to another signal, presumably H_4 which occurs at higher temperatures.)

Another aspect that supports the interpretation as signal superposition is the change in capacitance during voltage pulse application: One always observes a slow increase in capacitance, corresponding to a capture of mi-

minority carriers irrespective of the direction of the subsequent emission signal (minority or majority carrier signal – positive or negative emission transient, respectively) as shown in figure 5.10(b). This means, in case of negative emission transients, the capacitance of the sample changes in the same direction during and after pulse application. Usually the latter is not expected to be observed in DLTS as charge carriers captured during application of the filling pulse have to be remitted afterwards, in order to reestablish the starting situation. Here, the change in capacitance ΔC_t of the sample is a good measure: comparing the values for ΔC before application of the voltage pulse and after return to equilibrium, no changes in ΔC due to the measurement cycle could be detected. As indicated in figure 5.10(b) by the dashed line as guidance for the eye, the change in capacitance of the device under test before and after perturbation is zero. Therefore, any irreversible changes can be excluded. However, due to its dependence on the free carrier concentration, the capture process is usually much faster than the emission process. At least, when capture mainly takes place in the neutral region of the device, it is often too fast to be monitored. Taking these considerations into account, the data could be explained by the occurrence of two processes, majority carrier and minority carrier capture, during application of the filling pulse. Here, it is assumed that the leakage current of the device provides the needed minority carriers. The majority capture rate would be too fast to be detected by the DLTS system used for the experiments presented so that only the capture of electrons is observed as a slow increase in capacitance. This might also explain why in RDLTS measurements only a minority carrier signal shows up, whereas in majority carrier DLTS one detects either a majority carrier or a minority carrier defect signal, depending on the height of the voltage pulse applied (see part two in figures 5.11(a) and (b)). However, the change in signal amplitude of E_1 on variation of the reverse bias voltage shown in figure 5.9(a) does not confirm this interpretation: The leakage current and therewith the minority carrier concentration increases with increasing reverse bias voltage applied so that the minority carrier signal E_1 should govern the DLTS spectrum when using high voltage pulses. In fact, figure 5.9(a) shows exactly the opposite behavior.

After having discussed different aspects of the results separately, some mechanisms addressed in literature will be discussed in view of the experimental findings. Considering the time constants that occur in these measurements, for example about 6 ms at 130 K for the signal E_1 resp. at 160 K for the signal H_1 in a Cu(In,Ga)Se₂ based solar cell with GGI equal to 0.50 (see figure 5.9(b)), mechanisms like formation of new defects can be excluded, even if one takes into account that for some of them their formation enthalpies depend on the position of the Fermi level [23]. Defect formation means that structural changes take place, and these should be much slower than the time constants observed, especially at temperatures below 200 K.

Electromigration of copper related defects, i.e., copper vacancies V_{Cu}^- and copper interstitials Cu_i^+ , is not very likely to induce the defect signals measured, either. Reference [115] shows that a persistent increase in device capacitance ascribed to electric field induced copper migration can, indeed, be achieved in two minutes at -2 V and 340 K, yet recovery of the original state is almost completed only after annealing for one hour at 340 K. So, in the temperature range below 200 K, one does not expect any dynamic response to the voltage pulses applied that is related to migration of copper. Referring to the different aspects discussed before, it becomes clear that a quite complex mechanism might be necessary to explain the experimental results obtained.

Although several models could be excluded in the preceding section, there are still two models left that might serve as explanation. However, as the examination of their validity requires a simulation program that can deal with capacitance transients which is not yet available, they can only be described here for future considerations. Both models assume a majority carrier deep level as original signal and the positive signal as a result of a sign inversion. The first one deals with an additional space charge capacitance in series to the "main" depletion region. This is an absolutely realistic assumption if one takes into account that presumably there exists an additional energy barrier at the back contact that comes into play only at lower temperatures. This barrier could be either a Schottky barrier at the molybdenum back contact of the device or an additional p-n junction located between the $Cu(In,Ga)Se_2$ and a $MoSe_2$ layer that develops during deposition of the absorber on the metal contact [17]. The idea is as follows: There is one defect level that is present in both space charge regions. If a voltage pulse is applied to the device under test, the trap occupation becomes — in principle — perturbed in both space charge regions, so that the resulting capacitance transient from a DLTS experiment, is actually a sum of two transients, the one stemming from the main depletion region, the other from the back contact depletion region. As these space charge regions connected in series are biased in opposite direction, the transients should have opposite signs, too. For instance, a reduction in reverse bias voltage induces carrier emission from trap states in the reverse biased space charge region whereas it leads to carrier capture in the forward biased one. One could now imagine that, depending on the specific measurement parameters, the one or the other transient dominates the resulting capacitive response, so that the DLTS signal finally obtained can be either positive or negative. First checks assuming two capacitors connected in series, where both cause exponential capacitance transients that have the same time constants, but opposite sign, were performed. The transients were calculated analytically using equation 4.11 and afterwards added up in the respective way ($1/C_{ges} = 1/C_{main} + 1/C_{back}$). However, within this simple check, a pulse height dependent sign change can only be achieved if

the capacitors have almost the same equilibrium capacitance values. The latter consequence is not very likely to happen in all devices investigated. On the other hand, the abrupt decrease in capacitance initially after application of the voltage pulse, as shown in figure 5.10(b), could be an indication for an increasing space charge layer at the back contact. So this possible explanation shall not be excluded completely, as the model assumed within the simple simulation so far might be oversimplified.

The second possible explanation shall actually not be described for a DLTS measurement but an impedance investigation. For this method the simulation program SCAPS 1-D is available [58]. Using this program, an inductive current contribution could be modeled under special conditions [116]. Unfortunately the transfer to transient techniques is momentarily not possible, as so far, no suitable simulation program is at hand. The description is restricted to the occurrence of negative capacitances in admittance measurements. The model is based on a leakage current driven by drift and diffusion that can be influenced by the occupation status of trap states: If one assumes a compensating majority carrier defect level with concentration in the same order of magnitude as the doping concentration and a potential barrier for majority carriers, the occupation of this defect level has a large influence on the band bending in vicinity of the barrier. Under reverse bias, the quasi-Fermi level of majority carriers is very close to the trap level in the near of the potential barrier, so that a small change in bias voltage can lead to a substantial change in trap occupation and therewith in band bending. If deep levels become unoccupied in this region, the effective doping decreases and the band bending is reduced, too. The diminished band bending leads to an increase in the space charge region extending from the barrier up to the neutral bulk. For a drift and diffusion driven leakage current, the distance between the barrier and the neutral bulk that the charge carriers have to transverse is the limiting factor. If the width of the depletion region is large, the leakage current is small as only few carriers manage their transition. However, if the position of the quasi-Fermi level is such that the deep levels in vicinity of the potential barrier are occupied, then the effective doping concentration is comparatively high, which leads to large band bending and therewith to a small width of depletion region. This means a comparatively large leakage current. Under these conditions, there is a substantial influence of the occupation status of the deep levels close to the potential barrier on the magnitude of the leakage current.

Now to the influence of this large compensating trap concentration on an impedance measurement (see also figure 6.1): Considering an a.c. voltage with small amplitude applied to a device with the aforementioned properties, the phase shift of the different current contributions induced by the modulation voltage shall be derived. The change in free carrier density at the edge of the depletion region δQ_{SCR} happens in phase with the a.c. voltage. The

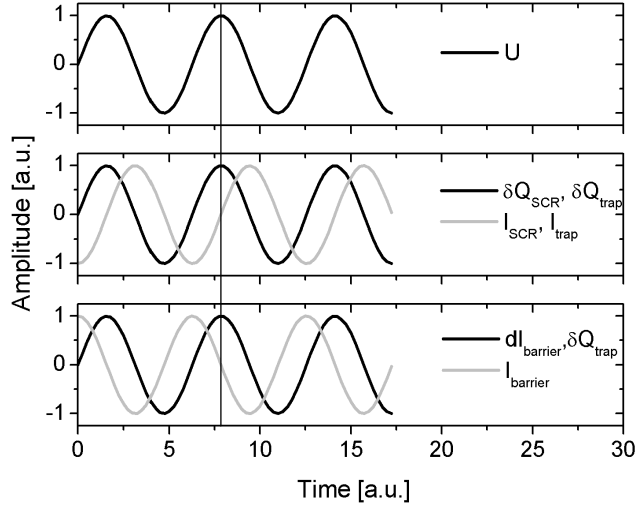


Figure 6.1: Illustration of how a large defect concentration can influence the leakage current of a device (driven by drift and diffusion) and induce an inductive current component.

modulation in occupation of the trap states at the position of the intersection point between the deep level with the quasi-Fermi level δQ_{trap} for simplicity is assumed to be in phase with the modulation, too. (See section 4.2 for a detailed description of the deep level response.) The resulting currents I_{SCR} and I_{trap} (as derivatives of the changes in charge with respect to time) are therefore $\pi/2$ ahead of the a.c. voltage. The change in leakage current over the barrier $dI_{barrier}$ is now again in phase with the change in "trap charge" δQ_{trap} . The resulting total current over the potential barrier $I_{barrier}$ is the time dependent integral of $dI_{barrier}$. $I_{barrier}$ is therewith $\pi/2$ behind $dI_{barrier}$ and the phase of the modulation voltage and therefore represents an inductive current contribution.

Although no final explanation for the peculiar behavior of the defect signals E_1 and H_1 can be given, several mechanisms could be excluded in view of the experimental findings. Referring to the various experiments performed, further investigations on this topic are recommended to focus on simulations to test the two different models proposed.

6.3 Peak width analysis of E_1 and H_1

Coming now to the peak width analysis reported in section 5.3.4, a possible explanation for the experimental findings shall be discussed. First, the peak

broadening observed is considered. There are several aspects that can cause a signal broadening in the DLTS versus temperature representation: (i) some distribution of activation energies, for instance, due to a band of closely spaced defect levels, (ii) "alloy broadening" effects, i.e., local fluctuations in material composition, (iii) electric field dependence of the emission rate or (iv) influence of the capture on the emission process because of a non-negligibly small transition region between depletion region and neutral bulk, etc. [86, 87, 88, 89, 91, 92].

The aspect of alloy broadening is discussed first, as one actually deals with absorber layers consisting of CuInSe₂ alloys with gallium. For statistical reasons, one actually expects for an A-B alloy system a dependence of the peak width on the concentration ratio $[A]/([A]+[B])$. The maximum broadening should occur at a ratio of 0.50. As this is obviously not the case for the data shown in figure 5.15(a) where the normalized peak width shows no clear dependence on GGI , this explanation can be excluded. However all other possible mechanisms require a detailed analysis of the defect signals themselves. An influence of the electric field for instance can be seen from a shift of the peak maximum or minimum (in the DLTS signal versus temperature representation) to lower temperatures with increasing height of voltage pulse as indicated in section 6.2. In case of non-negligible transition region, i.e., occurrence of capture in the Debye tail, the peak maximum or minimum shifts to higher temperatures with larger amplitude of voltage pulse as the influence of the capture rate becomes less and therefore the inverse time constant decreases. A band of defects usually is characterized by a peak broadening and a shift of the peak maximum or minimum to higher temperatures with increasing length of voltage pulse. Usually as a rule of thumb, it can be said that the higher the activation energy of a defect, the lower is the capture cross section. Therefore with increasing pulse length more and more defect levels with higher activation energies contribute to the signal so that the mean emission rate or activation energy describing this band increases, too. However the different forms of analysis cannot be performed on the special signals E_1 and H_1 because of their exceptional behavior. The origin of these defect signals has to be clarified to understand the experimental findings, otherwise an interpretation of the peak broadening determined is not possible.

As second aspect, the GGI dependence of the activation energies for E_1 and H_1 are addressed. As can be seen from figure 5.15(b), E_a decreases from CuInSe₂ based samples to those with a gallium content of 0.28. For samples with GGI equal to 0.50, the activation energies increase again and finally level off for devices with GGI larger than 0.50. It is interesting to note, that the decrease in activation energy up to a GGI of 0.28 and the minimum in activation energies for E_1 and H_1 correspond to the respective changes in solar cell efficiencies, which increase up to a gallium content of 0.28 and show

a maximum at GGI equal to 0.28. This correlation is, however, so far only a phenomenological result deserving further investigations.

Chapter 7

Conclusions

A systematic study of Cu-chalcopyrite based solar cells covering the whole indium-gallium alloy range with admittance and deep level transient spectroscopy was presented in order to determine the characteristic changes in defect spectra with varying gallium content. For the mixed absorber compositions, i.e., those containing both indium and gallium, in principle, the same deep levels were identified. In CIS and CGS devices, additional deep traps come into play. Concerning the unwanted breakdown of the open circuit voltage at $GGI \geq 0.3$, no detrimental defect that might be responsible for this phenomenon was detected. Considering that the capacitance DLTS measurement technique applied is bulk sensitive, it can be concluded that bulk defects are not decisive concerning the V_{OC} issue. The ranges of activation energies for the occurring defect signals were determined, too. However, due to signal overlap and other influences, the values given are only effective or apparent numbers.

In the temperature range below 200 K, two defect signals, E_1 and H_1 that are present for all GGI investigated, are detected. Detailed DLTS variation measurements like variation of the reverse bias voltage U_R or variation of the height of voltage pulse applied to the device under test, were performed on these signals and revealed remarkable properties: Depending on the respective measurement parameters applied, either the majority carrier or the minority carrier defect signal or a combination of both was detected. These findings could be explained by defect concentration profiles. The defect signals E_1 and H_1 exhibit remarkably similar trap parameters which might indicate that they stem from the same defect level. By exclusion of several straightforward explanations it was demonstrated that an elaborate ansatz might be necessary to cope with all observations made. Two remaining explanations were presented, the one based on an additional space charge region at the back contact of the solar cell, the other assuming a large concentration of compensating defects that influence the band bending close to the CdS/CIGS interface and therewith the magnitude of leakage current.

Moreover, an analysis of the relative peak width for the two trap signals E_1 and H_1 was presented, too. In both cases, the peaks are somewhat broadened compared to the theoretical values, but no clear connection between the peak width and the gallium content is visible. However, the activation energies of these signals show a GGI dependency: Up to a GGI of 0.28, E_a decreases and then levels off at a somewhat higher value for the samples with larger gallium content. A detailed interpretation of the experimental findings is, however, not possible, until the reason for the exceptional behavior of these defect signals can be determined. Interestingly, the decrease in activation energy up to a GGI of 0.28 corresponds remarkably well to the respective increase in solar cell efficiency up to the same gallium content.

For future investigations on the issue of V_{OC} breakdown, one should turn to interface sensitive measurement techniques as the influence of the bulk material properties on this issue could be excluded. Concerning electrically active defects, one might for example use the current or charge DLTS techniques [117, 118, 119]. Clarifying the origin of the defect signals is also an interesting open question. Here further results might only be achieved by simulations, so the development of a program that is able to calculate transient changes in any form is desirable.

Bibliography

- [1] K. Ramathan, M. A. Contreras, C. L. Perkins, S. Asher, F. S. Hasoon, J. Keane, D. Young, M. Romero, W. Metzger, R. Noufi, J. Ward, and A. Duda, *Prog. Photovolt. Res. Appl.* **11**, 225 (2003).
- [2] M. Powalla, B. Dimmler, R. Schaeffler, G. Voorwinden, U. Stein, H.-D. Mohring, F. Kessler, and D. Hariskos, in *Proc. 19th European Photovoltaic Solar Energy Conf.*, edited by W. Hoffmann, J.-L. Bal, H. Ossenbrink, W. Palz, and P. Helm, p. 1663, WIP, Munich, 2004.
- [3] C. A. D. Ricón, E. Hernández, M. I. Alonso, M. Garriga, S. M. Wasim, C. Ricón, and M. León, *Mater. Chem. Phys.* **70**, 300 (2001).
- [4] W. N. Honeyman, *J. Phys. Chem. Solids* **30**, 1935 (1969).
- [5] L. I. Berger and V. Prochukhan, *Ternary Diamond-Like Semiconductors*, p. 49, Consultants Bureau, New York, 1969.
- [6] B. Tell, J. L. Shay, and H. M. Kasper, *Phys. Rev. B* **4**, 2463 (1971).
- [7] J. E. Jaffe and A. Zunger, *Phys. Rev. B.* **28**, 5822 (1983).
- [8] U. Rau and H.-W. Schock, *Appl. Phys. A* **69**, 131 (1999).
- [9] L. Kronik, D. Cahen, and H. W. Schock, *Adv. Mater.* **10**, 31 (1998).
- [10] S. H. Wei, S. B. Zhang, and A. Zunger, *J. Appl. Phys.* **10**, 7214 (1999).
- [11] M. Bodegård, L. Stolt, and J. Hedström, in *Proc 12th European Photovoltaic Solar Energy Conf.*, edited by R. Hill, W. Palz, and P. Helm, StephensF, Bedford, UK.
- [12] D. Wolf, G. Müller, W. Stetter, and F. Karg, in *Proc. 2nd World Conf. on Photovolt. Energy Conf.*, edited by J. Schmid, H. A. Ossenbrink, P. Helm, H. Ehmman, and E. D. Dunlop, p. 2426, E. C. Joint Res. Centre, Luxembourg, 1998.

- [13] M. Ruckh, D. Schmid, M. Kaiser, R. Schäßler, T. Walter, and H. W. Schock, in *Proc. 1st World Conf. on Solar Energy Conversion*, p. 156, IEEE, New York, 1994.
- [14] V. Lyahovitskaya, Y. Feldman, K. Gartsman, H. Cohen, C. Cytermann, and D. Cahen, *J. Appl. Phys.* **91**, 4205 (2002).
- [15] D. Rudmann, G. Bilger, M. Kaslin, F. J. Haug, and H. Zogg, *Thin Solid Films* **431**, 37 (2003).
- [16] J. H. Scofield, A. Duda, D. Albin, B. L. Ballard, and P. Predecki, *Thin Solid Films* **260**, 26 (1995).
- [17] M. Nishitani, N. Kohara, T. Negami, and T. Wada, *Jpn. J. Appl. Phys.* **37**, L71 (1998).
- [18] L. Assmann, J. C. B. A. Drici, C. Amory, E. Halgand, and M. Morsli, *Appl. Surface Science* **246**, 159 (2005).
- [19] <http://www.superstrate.net/pv/cigs.html>, 2005.
- [20] S. B. Zhang, S.-H. Wei, and A. Zunger, *Phys. Rev. Lett.* **78**, 4059 (1997).
- [21] R. Herberholz, U. Rau, H. W. Schock, T. Haalboom, T. Gödecke, F. Ernst, C. Beilharz, and D. C. K. W. Benz, *Eur. Phys. J. AP* **6**, 131 (1999).
- [22] R. Noufi, R. Axton, C. Herrington, and S. K. Deb, *Appl. Phys. Lett.* **45**, 668 (1984).
- [23] S. B. Zhang, S.-H. Wei, A. Zunger, and H. Katayama-Yoshida, *Phys. Rev. B* **57**, 9642 (1998).
- [24] S. Schuler, S. Siebentritt, S. Nishiwaki, N. Rega, J. Beckmann, S. Brehme, and M. Lux-Steiner, *Phys. Rev. B* **69**, 045210 (2004).
- [25] I. Dirnstorfer, M. T. Wagner, D. M. Hofmann, M. D. Lampert, F. Karg, and B. K. Meyer, *Phys. Stat. Sol. (a)* **168**, 163 (1998).
- [26] M. Kemell, M. Ritala, and M. Leskela, *Critical Rev. in Solid State Mater. Sci.* **30**, 31 (2005).
- [27] G. D. Mooney, A. M. Hermann, J. R. Tuttle, D. S. Albin, and R. Noufi, *Appl. Phys. Lett.* **58**, 2678 (1991).
- [28] K. Zweibel, H. S. Ullal, and R. L. Mitchell, in *Proc. 21st IEEE Photovolt. Spec. Conf.*, p. 458, IEEE, New York, 1990.

- [29] N. G. Dhere, M. C. Lourenco, R. G. Dhere, and L. L. Kazmerski, *Solar Cells* **13**, 59 (1984).
- [30] M. A. Contreras, J. Tuttle, A. Gabor, A. Tennant, S. Ramanathan, S. Asher, A. Franz, J. Keane, L. Wang, J. Scofield, and R. Noufi, in *Proc. 24th IEEE Photovolt. Spec. Conf.*, p. 68, IEEE, New York, 1994.
- [31] J. Kessler, C. Chityuttakan, J. Lu, J. Scholdstrom, and L. Stolt, *Prog. Photovolt. Res. Appl.* **11**, 319 (2003).
- [32] T. Dullweber, G. Hanna, W. Shams-Kolahi, A. Schwartzlander, M. A. Contreras, R. Noufi, and H. W. Schock, *Thin Solid Films* **361-362**, 478 (2000).
- [33] J. R. Tuttle, D. S. Albin, and R. Noufi, *Solar Cells* **30**, 21 (1991).
- [34] M. Powalla, G. Voorwinden, and B. Dimmler, in *Proc. 14th European Photovoltaic Solar Energy Conf.*, edited by H. A. Ossenbrink, P. Helm, and H. Ehmann, p. 1270, Stephens, Bedford, UK, 1997.
- [35] D. Liao and A. Rockett, *Appl. Phys. Lett.* **82**, 2829 (2003).
- [36] H.-S. Han, A. M. Hermann, F. S. Hasoon, H. A. Al-Thani, and D. H. Levi, *Appl. Phys. Lett.* **85**, 576 (2004).
- [37] D. Liao and A. Rockett, *J. Appl. Phys.* **93**, 9380 (2003).
- [38] C.-S. Jiang, F. S. Hasoon, H. R. Moutinho, H. A. Al-Thani, and M. J. Romero, *Appl. Phys. Lett.* **82**, 127 (2003).
- [39] U. Rau, D. Braunger, R. Herberholz, H. W. Schock, J. F. Guillemoles, L. Kronik, and D. Cahen, *J. Appl. Phys.* **86**, 497 (1999).
- [40] D. Schmid, M. Ruckh, F. Grunwald, and H.-W. Schock, *J. Appl. Phys.* **73**, 2902 (1993).
- [41] N. G. Dhere, D. L. Waterhouse, K. B. Sundaram, O. Melendez, N. R. Parik, and B. Patnaik, *J. Mater. Sci. — Mater. Electronics* **6**, 52 (1995).
- [42] T. Nakada, K. Furumi, and A. Kunioka, *IEEE Transactions on Electron Devices* **46**, 2097 (1999).
- [43] A. Ennaoui, *Can. J. Phys.* **77**, 723 (1999).
- [44] J. Kessler, K. O. Velthaus, M. Ruckh, R. Laichinger, H. W. Schock, D. Lincot, R. Ortega, and J. Vedel, in *Proc. 6th Intern. Photovolt. Science Eng. Conf.*, edited by B. K. Das and S. N. Singh, p. 1005, Oxford Publ., New Delhi, 1992.

- [45] S. M. Sze, *Physics of Semiconductor Devices*, Wiley, New York, 1981.
- [46] J. Mass, P. Bhattacharya, and R. S. Katiyar, *Mater. Sci. Engin. B* **103**, 9 (2003).
- [47] U. Rau and U. Schmidt, *Thin Solid Films* **387**, 141 (2001).
- [48] D. Eich, U. Herber, U. Groth, U. Stahl, C. Heske, M. Marsi, M. Kishinova, W. Riedel, R. Fink, and E. Umbach, *Thin Solid Films* **361-362**, 258 (2000).
- [49] H. Hahn, G. Frank, W. Klingler, A. D. Meyer, and G. Storer, *Anorgan. und Allgem. Chemie* **271**, 153 (1953).
- [50] R. Herberholz, V. Nadenau, U. Rühle, H.-W. Schock, and B. Dimmler, *Solar Energy Mater. Solar Cells* **49**, 227 (1997).
- [51] W. N. Shafarman, R. Klenk, and B. E. McCandless, *J. Appl. Phys.* **79**, 7324 (1996).
- [52] H. W. Schock, in *Proc. 12th European Photovolt. Solar Energy Conf.*, edited by R. Hill, W. Palz, and P. Helm, p. 944, Stephens, Bedford, UK, 1994.
- [53] J. M. Stewart, W. S. Chen, W. M. Devaney, and R. A. Mickelsen, in *Proc. 7th Intern. Conf. on Ternary and Multinary Compounds*, edited by S. K. Deb and A. Zunger, p. 59, Materials Research Society, Pittsburgh, PA, 1987.
- [54] T. Löher, W. Jägermann, and C. Pettenkofer, *J. Appl. Phys.* **72**, 731 (1995).
- [55] T. Schulmeyer, R. Hunger, A. Klein, and W. Jägermann, *Appl. Phys. Lett.* **84**, 3067 (2004).
- [56] M. Turcu, I. M. Kötschau, and U. Rau, *Appl. Phys. A* **73**, 769 (2001).
- [57] S. H. Wei, S. B. Zhang, and A. Zunger, *Appl. Phys. Lett.* **72**, 3199 (1998).
- [58] M. Burgelman, P. Nollet, and S. Degraeve, *Thin Solid Films* **361-362**, 527 (2000).
- [59] I. E. Beckers, U. Fiedeler, S. Siebentritt, and M. C. Lux-Steiner, *Thin Solid Films* **431**, 205 (2003).
- [60] V. Nadenau, U. Rau, A. Jasenek, and H. W. Schock, *J. Appl. Phys.* **87**, 584 (2000).

- [61] R. R. Philip, B. Pradeep, G. S. Okram, and V. Ganesan, *Semicond. Sci. Technol.* **19**, 798 (2004).
- [62] J. T. Heath, J. D. Cohen, and W. N. Shafarman, *J. Appl. Phys.* **95**, 1000 (2004).
- [63] R. Herberholz, M. Igalson, and H. W. Schock, *J. Appl. Phys.* **83**, 318 (1998).
- [64] M. Turcu, I. M. Kötschau, and U. Rau, *J. Appl. Phys.* **91**, 1391 (2002).
- [65] A. Jasenek, U. Rau, V. Nadenau, and H. W. Schock, *J. Appl. Phys.* **87**, 594 (2000).
- [66] G. Hanna, A. Jasenek, U. Rau, and H. W. Schock, *Thin Solid Films* **387**, 71 (2001).
- [67] J. T. Heath, J. D. Cohen, and W. N. Shafarman, *J. Appl. Phys.* **95**, 1000 (2004).
- [68] D. L. Young and R. S. Crandall, *Appl. Phys. Lett.* **83**, 2363 (2003).
- [69] W. Schottky, *Zeitschr. Physik* **41**, 570 (1938).
- [70] W. Shockely, J. Bardeen, and W. H. Brattain, *Science* **108**, 678 (1948).
- [71] P. Würfel, *Physik der Solarzelle*, Spektrum Akademischer Verlag, Heidelberg, 1995.
- [72] W. Shockely and W. T. Read, *Phys. Rev.* **87**, 835 (1952).
- [73] R. N. Hall, *Phys. Rev.* **87**, 387 (1952).
- [74] P. Blood and J. Orton, *The Electrical Characterization of Semiconductors: Majority Carriers and Electron States*, Academic Press, London, 1992.
- [75] D. V. Lang, *J. Appl. Phys.* **45**, 3023 (1974).
- [76] I. Thurzo, R. Beyer, and D. R. T. Zahn, *Semicond. Sci. Technol.* **15**, 378 (2000).
- [77] D. V. Lang, *Topics in Applied Physics: Thermally Stimulated Relaxation in Solids*, p. 102, Springer, Berlin, 1979.
- [78] G. P. Li and K. L. Wang, *Appl. Phys. Lett.* **42**, 838 (1983).
- [79] G. P. Li and K. L. Wang, *J. Appl. Phys.* **57**, 1016 (1983).

- [80] L. Dobaczewski, P. Kaczor, M. Missous, A. R. Peaker, and Z. R. Zytckiewicz, *Phys. Rev. Lett.* **68**, 2508 (1992).
- [81] S. A. Studenikin, N. Golego, and M. Cocivera, *Semicond. Sci. Technol.* **13**, 1383 (1998).
- [82] S. W. Provencher, *Comp. Phys. Commun.* **27**, 213 (1982).
- [83] S. W. Provencher, *Comp. Phys. Commun.* **27**, 229 (1982).
- [84] A. A. Istratov, O. F. Vyvenko, H. Hieslair, and E. R. Weber, *Meas. Sci. Technol.* **9**, 477 (1998).
- [85] J. D. Cohen and D. V. Lang, *Phys. Rev. B* **25**, 5321 (1982).
- [86] P. Omling, L. Samuelson, and G. H. Grimmeis, *J. Appl. Phys.* **54**, 5117 (1983).
- [87] W. Schröter, H. Hedemann, V. Kveder, and F. Riedel, *J. Phys. C* **14**, 13047 (2002).
- [88] J. M. Noras and H. R. Szawelska, *J. Phys. C* **15**, 2001 (1982).
- [89] D. Pons, *J. Appl. Phys.* **55**, 3644 (1984).
- [90] M. C. Chen, D. V. Lang, W. C. Dautremont-Smith, A. M. Sergent, and J. P. Harbison, *Appl. Phys. Lett.* **44**, 790 (1984).
- [91] G. Vincent, A. Chantre, and D. Bois, *J. Appl. Phys.* **50**, 5484 (1979).
- [92] P. Zabierowski and M. Igalson, *Thin Solid Films* **361-362**, 268 (2000).
- [93] A. Broniatowski, A. Blossé, P. C. Srivastava, and J. C. Bourgoin, *J. Appl. Phys.* **54**, 2907 (1983).
- [94] N. Fourches, *Appl. Phys. Lett.* **58**, 364 (1991).
- [95] F. D. Auret and M. Nel, *J. Appl. Phys.* **61**, 2546 (1987).
- [96] Y. Chen, G. Chen, Y. Tian, and F. Lu, *Semicond. Sci. Technol.* **17**, 497 (2002).
- [97] R. Arora and A. Kumar, *Phys. Stat. Solidi (a)* **125**, 273 (1991).
- [98] H. Antoniadis and E. A. Schiff, *Phys. Rev. B.* **46**, 9482 (1992).
- [99] W. Meyer and H. Neldel, *Z. Tech. Phys.* **12**, 588 (1937).
- [100] A. Yelon and B. Movaghar, *Phys. Rev. Lett.* **65**, 618 (1990).

- [101] A. Wessel, *Transiente Störstellenspektroskopie an Cu(In,Ga)(S,Se)₂-Dünnschichtsolarzellen*, Diplomarbeit, Universität Oldenburg, 2002.
- [102] D. V. Lang, J. Appl. Phys. **45**, 3023 (1974).
- [103] C. Deibel, V. Dyakonov, J. Parisi, J. Palm, S. Zweigart, and F. Karg, in *Proc. 17th European Photovol. Solar Energy Conf.*, edited by B. McNellis, W. Palz, H. A. Ossenbrink, and P. Helm, p. 1229, WIP, Munich, 2002.
- [104] R. Herberholz, T. Walter, C. Müller, T. Friedlmeier, H. W. Schock, M. Saad, M. C. Lux-Steiner, , and V. Alberts, Appl. Phys. Lett. **69**, 2888 (1996).
- [105] C. Deibel, V. Dyakonov, and J. Parisi, Appl. Phys. Lett **82**, 3559 (2003).
- [106] R. Herberholz, M. Igalson, and H. W. Schock, J. Appl. Phys. **83**, 318 (1998).
- [107] A. Niemegeers, R. H. M. Burgelman, U. Rau, D. Hariskos, and H. W. Schock, Prog. Photovolt. Res. Appl. **668** (1998).
- [108] M. Igalson, M. Bodegård, L. Stolt, and A. Jasenek, Thin solid films **431-432**, 153 (2003).
- [109] M. Igalson and M. Edoff, Thin solid films **480-481**, 322 (2005).
- [110] C. Deibel, V. Dyakonov, and J. Parisi, Europhys. Lett. **66**, 399 (2004).
- [111] R. H. T. Walter and, C. Müller, and H. W. Schock, J. Appl. Phys. **80**, 4411 (1996).
- [112] M. Igalson and P. Zabierowski, Thin Solid Films **361-362**, 371 (2000).
- [113] J. T. Heath, J. D. Cohen, W. N. Shafarman, D. X. Liao, and A. A. Rocket, Appl. Phys. Lett. **80**, 4540 (2002).
- [114] V. Mertens, J. Parisi, M. Köntges, and R. Reineke-Koch, in *Proc. 19th European Photovoltaic Solar Energy Conf.*, edited by W. Hoffmann, J.-L. Bal, H. Ossenbrink, W. Palz, and P. Helm, p. 1925, WIP, Munich, 2004.
- [115] J.-F. Guillemoles, U. Rau, L. Kronik, H.-W. Schock, and D. Cahen, Adv. Mater. **11**, 957 (1999).
- [116] M. Köntges, unpublished (2005).

- [117] B. W. Wessels, *J. Appl. Phys.* **61**, 1131 (1976).
- [118] K. L. Kirov and K. B. Radev, *Phys. Stat. Solidi (a)* **63**, 711 (1981).
- [119] J. W. Farmer, C. D. Lamp, and J. M. Meese, *Appl. Phys. Lett.* **41**, 1063 (1982).

Danksagung

Ich möchte mich hier gern bei allen bedanken, die maßgeblich zum Gelingen dieser Arbeit beigetragen haben. Mein Dank gilt:

- Jürgen Parisi, der mir die Durchführung dieser Arbeit ermöglicht hat, für die stete Unterstützung und Aufmunterung.
- Rolf Reineke-Koch und Marc Köntges vom ISFH für die engagierte Betreuung mit vielen Diskussionen und zahlreichen Anregungen.
- Carsten Deibel für seine Hilfe bei der thematischen Einarbeitung und vor allem für die Bereitschaft, immer einen guten Rat zu geben.
- meiner ehemaligen Diplomandin Eva Schlenker für die gute und angenehme Zusammenarbeit und die Unterstützung an der "CIGS-Front".
- meiner langjährigen Bürokollegin Elizabeth von Hauf für die Begleitung durch alle Phasen der Doktorarbeit...
- allen aktuellen und ehemaligen Kollegen der Arbeitsgruppen Photovoltaik und Epkos: Susanne Böger, Britta Bohnenbuck, Zivayi Chiguvare, Dana Chirvase, Elzbieta Chojnowski, Vladimir Dyakonov, Andrea Geisler, Leonid Govor, Hans Holtdorf, Wilhelms Jürgens. Achim Kittel, Martin Knipper, Joanna Kolny-Olesiak, Holger Koch, Marion Luttmann, Mattias Macke, Tanja Miesner, Marco Munzel, Michael Pientka, Jens Reemts, Ingo Riedel, Martin Schreiner, Johannes Sieger, Stefan Trotzky, Arne Wessel, Uli Wischnath. Vielen Dank für das freundschaftliche und angenehme Arbeitsklima.
- Gottfried Bauer, Levent Gütayi und Tim Jürgens für interessante Gespräche und Ideenaustausch.
- Stephan Ulrich für fachliche Diskussion.
- Robert Kniese und Wolfram Witte (ZSW) für die Bereitstellung der Proben.
- den Projektpartnern des Hochspannungsnetzwerkes, für die gute Zusammenarbeit und hilfreiche Anregungen.
- meinen Eltern, meinen Geschwistern Eva und Alexander, Jörn und meinem Freund Christoph: für den unerschütterlichen Rückhalt und so vieles mehr.

Lebenslauf

Verena Maren Mertens

geboren am 09.03.1978
in Paderborn

Schulbildung

1984 bis 1988 Grundschule Marienloh, Paderborn
1988 bis 1997 Gymnasium St. Michael, Paderborn

Studium

10/1997 bis 05/2002 Studium an der Westfälischen Wilhelms-Universität
Münster
Studienfach Chemie (Diplom)
05/2000 Vordiplom
10/2000 bis 04/2001 Auslandsaufenthalt an der University of California
in Santa Barbara, USA
05/2002 Diplom

Promotion

6/2002 bis 12/2005 Promotionsstudium an der Carl von Ossietzky
Universität Oldenburg
Thema: Capacitance spectroscopy on copper indium
diselenide based solar cells

Erklärung

Hiermit versichere ich, dass ich diese Arbeit selbständig verfasst und keine anderen als die angegebenen Hilfsmittel verwendet habe. Die Teile dieser Dissertation wurden bereits veröffentlicht.

Oldenburg, 7.10.2005

Verena Mertens